Article

A bioorthogonal system reveals antitumour immune function of pyroptosis

https://doi.org/10.1038/s41586-020-2079-1

Received: 26 July 2019

Accepted: 4 February 2020

Published online: 11 March 2020

Check for updates

Qinyang Wang[1,7], Yupeng Wang[2,3,7], Jingjin Ding[3,4], Chunhong Wang[1], Xuehan Zhou[1], Wenqing Gao[3], Huanwei Huang[3], Feng Shao[2,3,5]✉ & Zhibo Liu[1,6]✉

Bioorthogonal chemistry capable of operating in live animals is needed to investigate biological processes such as cell death and immunity. Recent studies have identified a gasdermin family of pore-forming proteins that executes inflammasome-dependent and -independent pyroptosis[1–5]. Pyroptosis is proinflammatory, but its effect on antitumour immunity is unknown. Here we establish a bioorthogonal chemical system, in which a cancer-imaging probe phenylalanine trifluoroborate (Phe-BF_3) that can enter cells desilylates and 'cleaves' a designed linker that contains a silyl ether. This system enabled the controlled release of a drug from an antibody–drug conjugate in mice. When combined with nanoparticle-mediated delivery, desilylation catalysed by Phe-BF_3 could release a client protein—including an active gasdermin—from a nanoparticle conjugate, selectively into tumour cells in mice. We applied this bioorthogonal system to gasdermin, which revealed that pyroptosis of less than 15% of tumour cells was sufficient to clear the entire 4T1 mammary tumour graft. The tumour regression was absent in immune-deficient mice or upon T cell depletion, and was correlated with augmented antitumour immune responses. The injection of a reduced, ineffective dose of nanoparticle-conjugated gasdermin along with Phe-BF_3 sensitized 4T1 tumours to anti-PD1 therapy. Our bioorthogonal system based on Phe-BF_3 desilylation is therefore a powerful tool for chemical biology; our application of this system suggests that pyroptosis-induced inflammation triggers robust antitumour immunity and can synergize with checkpoint blockade.

As a positron emission tomography (PET) imaging probe for cancers, [^{18}F]Phe-BF_3 has a comparable sensitivity to—but a higher specificity than—[^{18}F]fluorodeoxyglucose[6–8]. Free fluoride, which is a deprotection agent in organic synthesis[9], catalyses efficient desilylation. We wondered whether Phe-BF_3 could also induce desilylation, and whether it could be developed into a bioorthogonal system for tumour-selective manipulation. To this end, we designed an *ortho*-carbamoylmethylene silyl-phenolic ether system attached to a client molecule, coumarin (Fig. 1a, Extended Data Fig. 1a). Desilylation of this system will cause the release of free coumarin, which becomes fluorescent (Extended Data Fig. 1b). We began with the *tert*-butyldimethyl silyl (TBS) group, and synthesized TBSO–coumarin with incorporation of a *para*-*N*,*N*-dimethylaminoacetamide for conjugation to a potential carrier (Fig. 1a, Extended Data Fig. 1a–c). Upon incubation with Phe-BF_3, TBSO–coumarin released fluorescent coumarin and the reaction-rate constant was comparable to that of sodium fluoride (Fig. 1b, Extended Data Fig. 2a–c). TBSO–coumarin did not react with hydrogen peroxide, glutathione or other biologically relevant anions (Extended Data Fig. 2b). In human BGC823 cells transfected with TBSO–coumarin, treatment with Phe-BF_3 resulted in strong coumarin fluorescence (Fig. 1c) Thus, desilylation catalysed by Phe-BF_3 can operate within live cells.

Antibody–drug conjugates hold promise in anticancer therapy[10], but suffer from an uncontrolled and inefficient release of the drug. We applied Phe-BF_3 desilylation to an antibody–drug conjugate system. Specifically, we used silyl-ether (TBS)-containing carbamate (SEC) to conjugate monomethyl auristatin E (MMAE) to trastuzumab (anti-HER2 antibody) (Fig. 1d, Extended Data Figs. 1e, 2d–f). Phe-BF_3 incubation caused about 90% MMAE release from the MMAE–SEC–trastuzumab conjugate (Extended Data Fig. 2g, h). Trastuzumab–SEC–MMAE incorporating trastuzumab labelled with zirconium-89 (^{89}Zr) showed expected tumour-targeting in nude mice grafted with HER2-positive BGC823 cells (Fig. 1e, Extended Data Fig. 2i, j). As previously reported[7,8,11], [^{18}F]Phe-BF_3 exhibited tumour uptake and retention; the concentration of [^{18}F]Phe-BF_3 in the tumour was much higher than in other tissues, and was also higher than the concentration of trastuzumab–SEC–MMAE in the tumour (Fig. 1e, Extended Data Fig. 2k, l). Marked release of MMAE in the tumour was detected when trastuzumab–SEC–MMAE and Phe-BF_3 were injected into the same mouse (Fig. 1f). Thus, our bioorthogonal system based on Phe-BF_3 desilylation enables the controlled and efficient release of the drug from an antibody–drug conjugate.

To optimize this system, we diversified the TBS group in the coumarin conjugate into triethylsilyl (TES) or triisopropyl silyl (TIPS) (Extended

[1]Beijing National Laboratory for Molecular Sciences, Radiochemistry and Radiation Chemistry Key Laboratory of Fundamental Science, College of Chemistry and Molecular Engineering, Peking University, Beijing, China. [2]Research Unit of Pyroptosis and Immunity, Chinese Academy of Medical Sciences, Beijing, China. [3]National Institute of Biological Sciences, Beijing, China. [4]National Laboratory of Biomacromolecules, Institute of Biophysics, Chinese Academy of Sciences, Beijing, China. [5]Tsinghua Institute of Multidisciplinary Biomedical Research, Tsinghua University, Beijing, China. [6]Peking-Tsinghua Center for Life Sciences, Peking University, Beijing, China. [7]These authors contributed equally: Qinyang Wang, Yupeng Wang. ✉e-mail: shaofeng@nibs.ac.cn; zbliu@pku.edu.cn

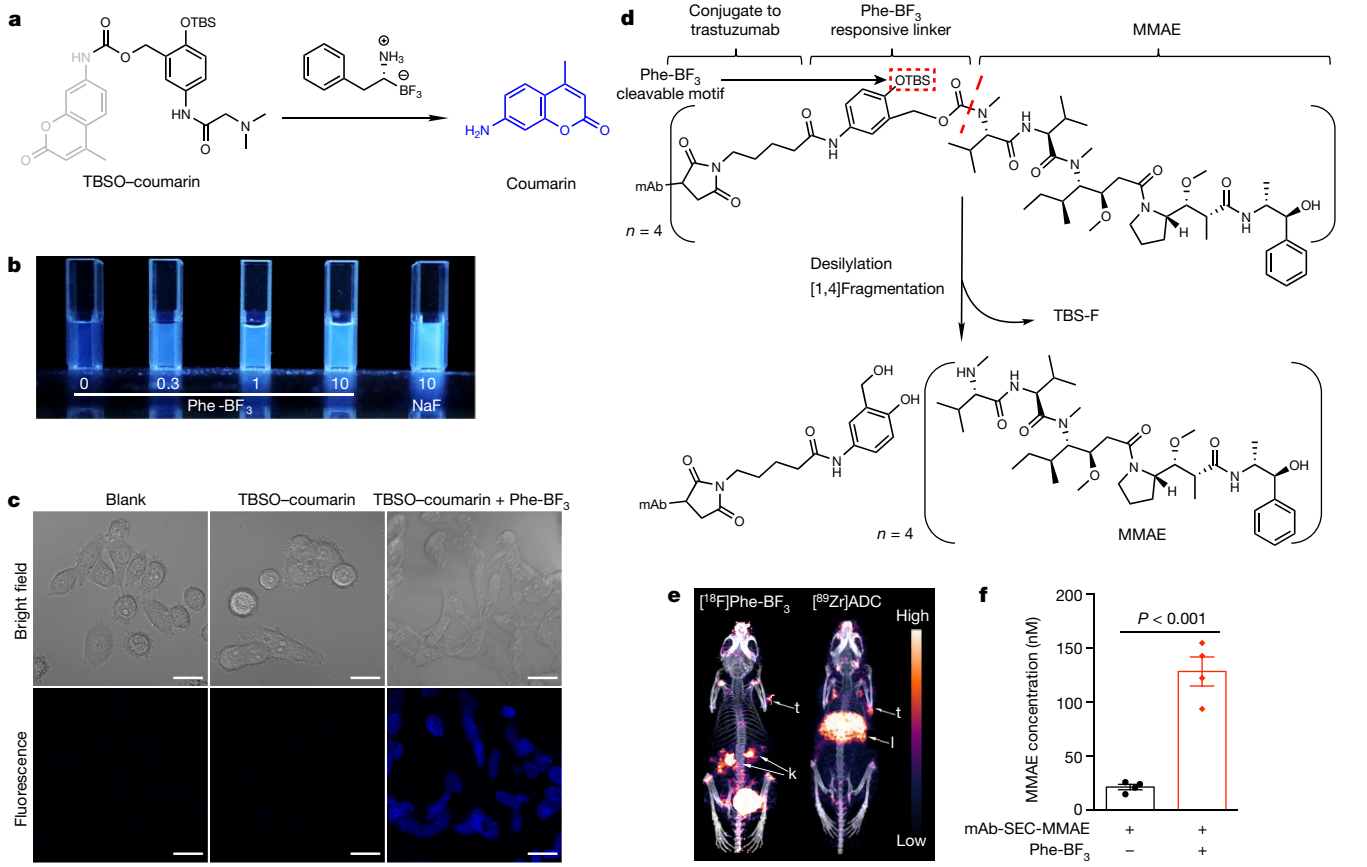

Fig. 1 | Desilylation bioorthogonal chemistry and its application to an antibody–drug conjugate. a, Schematic of the release of fluorescent coumarin from TBSO–coumarin, induced by Phe-BF_3 desilylation. **b**, TBSO–coumarin was reacted with the indicated relative amounts of Phe-BF_3 or NaF. **c**, Confocal images of BGC823 cells that were transfected with TBSO–coumarin and then treated with Phe-BF_3. Scale bars, 20 μm. **d**, Design of the trastuzumab (mAb)–SEC–MMAE conjugate, and MMAE release induced by Phe-BF_3 desilylation. **e**, **f**, Nu/Nu mice were implanted subcutaneously with BGC823 cells. **e**, PET-computed tomography images of mice intravenously injected with [^{18}F]Phe-BF_3 or [^{89}Zr]trastuzumab–SEC–MMAE (marked as ADC). t, tumour; l, liver; k, kidney. **f**, Mice were injected with trastuzumab (mAb)–SEC–MMAE alone (4.5 mg per kg body weight (kg^{-1})) or additionally with Phe-BF_3 (15 mg kg^{-1}). Tumour concentrations of MMAE are mean ± s.e.m. $n = 4$ mice, two-tailed unpaired Student's t-test. Data are representative of two (**c**, **f**) or three (**b**, **e**) independent experiments.

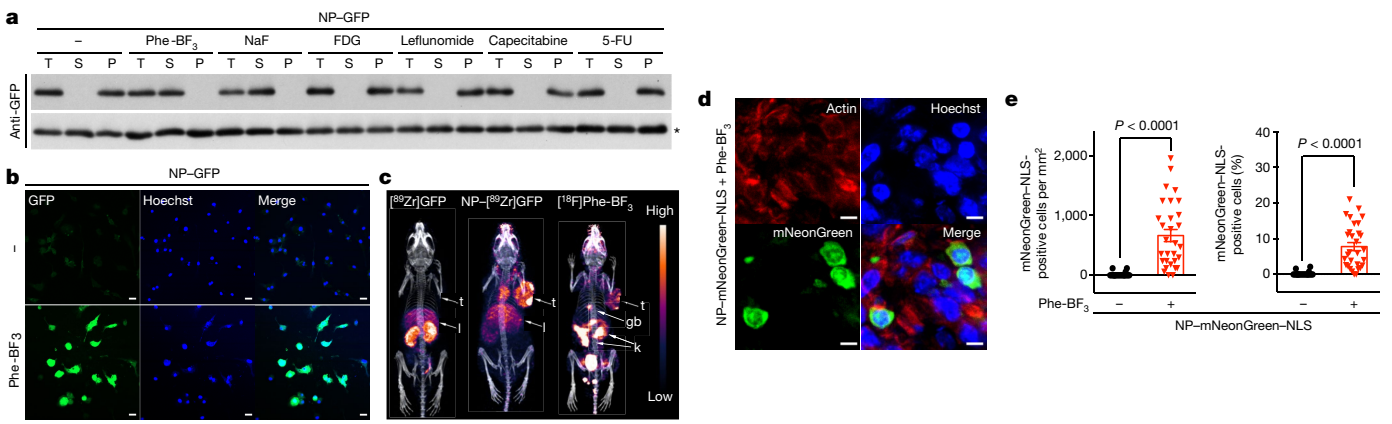

Fig. 2 | Phe-BF_3 desilylation releases GFP from TES-linked NP–GFP with tumour selectivity in mice. a, NP–GFP was treated with Phe-BF_3 or another indicated fluorine compound. The reactions were centrifuged (Extended Data Fig. 4b). P, pellet; S, supernatant; T, total; *, loading control sampled before centrifugation. **b**, Confocal fluorescence images of primary BMDMs treated with NP–GFP (1 mg ml^{-1}) for 24 h, followed by Phe-BF_3 (100 μM) for another 24 h. Scale bars, 20 μm. **c**–**e**, BALB/c mice were implanted subcutaneously with 4T1 cancer cells. **c**, PET-computed tomography images of mice intravenously injected with [^{89}Zr]GFP, NP–[^{89}Zr]GFP or [^{18}F]Phe-BF_3. gb, gallbladder. **d**, **e**, Mice were injected with NP–mNeonGreen–NLS. **d**, Confocal fluorescence images of a tumour section, magnified from Extended Data Fig. 4i. Scale bars, 5 μm. **e**, Numbers and percentages of mNeonGreen–NLS-positive cells in the tumour. $n = 22$ fields from 2 mice injected with NP–mNeonGreen–NLS or $n = 30$ fields from 4 mice injected with NP–mNeonGreen–NLS and Phe-BF_3. Data shown as mean ± s.e.m. (two-tailed unpaired Student's t-test) (**e**) and representative of two (**b**–**e**) or three (**a**) independent experiments.

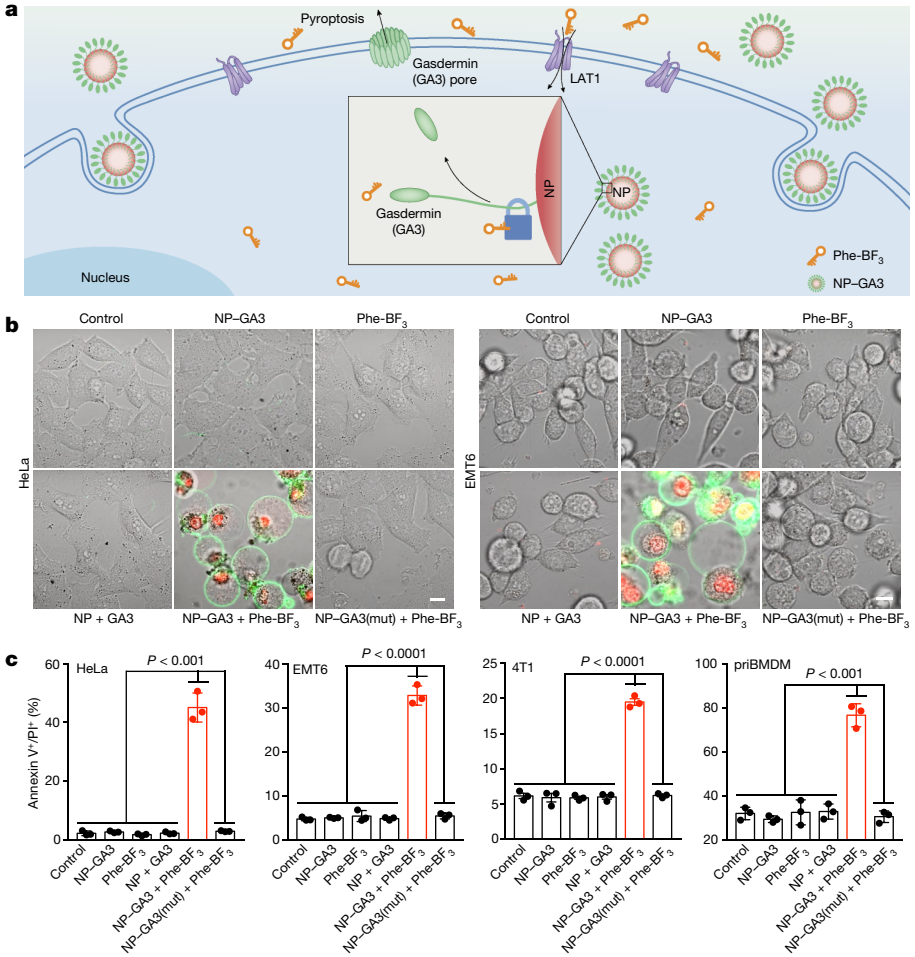

Fig. 3 | Phe-BF_3 desilylation releases gasdermin from NP–GSDMA3 to induce pyroptosis. a, Cartoon of the experimental design. Purified GSDMA3(N + C) was conjugated to a nanoparticle to obtain NP–GSDMA3. **b**, **c**, HeLa, EMT6 or 4T1 cells, or primary BMDMs, were treated as indicated. NP + GSDMA3, nanoparticles mixed with the GSDMA3(N + C) complex. **b**, Confocal images of the treated HeLa and EMT6 cells. Scale bars, 20 μm. Propidium iodide (PI) and annexin V–fluorescein isothiocyanate (FITC) were added to the cells 15 min before imaging. **c**, Flow-cytometry measurements of cells positive for propidium iodide and annexin V. priBMDM, primary BMDM. Mean ± s.d. from three independent replicates, two-tailed unpaired Student's *t*-test. GA3, GSDMA3(N + C). All data are representative of three independent experiments.

Data Figs. 1a, c, 3a). Although TIPSO–coumarin resisted desilylation catalysed by Phe-BF_3, TESO–coumarin was desilylated much more efficiently (Extended Data Fig. 3b–e). Differential reactivity of the three silyl groups indicates a steric hindrance effect, echoing desilylation catalysed by sodium fluoride[12] (Extended Data Fig. 3e). At 10-mM concentration, the desilylation induced by Phe-BF_3 was completed instantly. Such a fast velocity suggests that the desilylation induced by Phe-BF_3 may proceed through direct fluoride transfer[13], as the generation of a free-fluoride intermediate from Phe-BF_3 features an extremely slow kinetics[14]. TESO–coumarin, TBSO–coumarin and TIPSO–coumarin all showed no spontaneous desilylation. TESO–coumarin was not desilylated by other agents, including fluorine-derived drugs (Extended Data Fig. 3f, g). Thus, of the groups we tested, TES is the best choice for the bioorthogonal system based on Phe-BF_3 desilylation.

Gold nanoparticles are a widely used drug-delivery vehicle[15]. A nanoparticle has a tumour preference owing to an enhanced permeability and retention effect in tumours, and a more-efficient internalization by cancer cells[16,17]. We attached the silyl-phenolic ether to nanoparticles (Extended Data Fig. 1d) and replaced the coumarin with green fluorescence protein (GFP) to generate nanoparticle (NP)–GFP (Extended Data Fig. 4a). Upon treatment with Phe-BF_3 or sodium fluoride (but not other fluorine-containing compounds), TES-linked NP–GFP released GFP completely and the release from TBS-linked NP–GFP was partial (Fig. 2a, Extended Data Fig. 4b, c). In HeLa cells, NP–GFP accessed the cytosol after damaging the endosomal membrane (Supplementary Videos 1, 2, Supplementary Fig. 1). HeLa cells, mouse mammary carcinoma EMT6 and 4T1 cells and primary mouse bone-marrow-derived macrophages (BMDMs) all expressed the LAT1 transporter for Phe-BF_3 (Extended Data Fig. 4d). Following treatment with NP–GFP, the addition of Phe-BF_3 induced evident GFP release in all the four types of cell; this did not occur with sodium fluoride, because it is not cell-permeable (Extended Data Fig. 4e). Owing to the loss of quenching by the nanoparticle[18], the released GFP became fluorescent (Fig. 2b). Thus, desilylation catalysed by Phe-BF_3 can release a functional protein from nanoparticles in mammalian cells.

Tumour enrichment of [^{18}F]Phe-BF_3 was also observed in BALB/c mice that were engrafted subcutaneously with 4T1 carcinoma cells (Fig. 2c). The remainder of the Phe-BF_3 was rapidly cleared via renal excretion. Unlike ^{89}Zr-labelled GFP ([^{89}Zr]GFP), nanoparticle-conjugated [^{89}Zr]GFP (NP–[^{89}Zr]GFP) started to accumulate in the tumour at 6 h after injection; its level reached a plateau at 18 h (Extended Data Fig. 4f, g). Although NP–[^{89}Zr]GFP was highly enriched in the liver, the distributions of NP–GFP and Phe-BF_3 overlap only in the tumour. To detect the desilylation of nanoparticle conjugates,

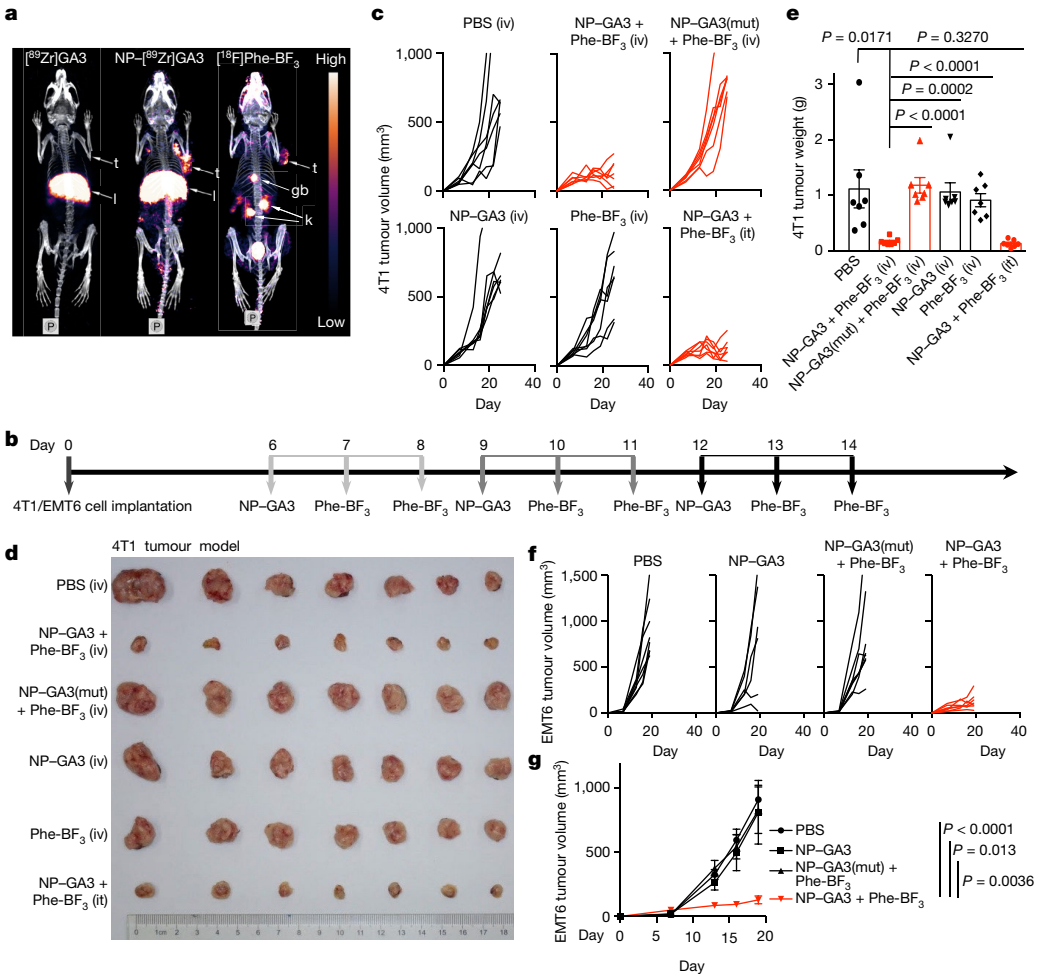

Fig. 4 | Treatment with NP–GSDMA3 and Phe-BF_3 causes tumour regression in mice. a, PET-computed tomography images of mice bearing 4T1 tumours that intravenously injected with [^{89}Zr]GSDMA3, NP–[^{89}Zr]GSDMA3 or [^{18}F]Phe-BF_3. **b**–**g**, BALB/c mice were implanted subcutaneously with 4T1 (**c**–**e**) or EMT6 (**f**, **g**) cells, followed by intravenous (iv) or intratumoural (it) injection of NP–GSDMA3 or Phe-BF_3 alone, or in combination. **b**, Treatment scheme. In **c**–**e**, $n = 7$ mice per group. In **f**, **g**, $n = 8$ mice for PBS and NP–GSDMA3(mut) + Phe-BF_3, 6 mice for NP–GSDMA3 and 7 mice for NP–GSDMA3 + Phe-BF_3. **c**, **f**, Tumour volume of an individual mouse. **d**, Photographs of representative tumours on day 26. **e**, **g**, Average tumour weight or volume. Mean ± s.e.m., two-tailed unpaired Student's *t*-test. GA3, GSDMA3(N + C). Data are representative of three (**c**–**e**) or two (**a**, **f**, **g**) independent experiments.

we replaced GFP with the brighter fluorescent protein mNeonGreen and introduced a nuclear-localization signal (NLS) to concentrate the released mNeonGreen fluorescence (Extended Data Fig. 4h). The 4T1 tumours in control mice showed no mNeonGreen fluorescence; about 15% of cells in tumours injected with Phe-BF_3 showed nuclear mNeonGreen signal (Fig. 2d, e, Extended Data Fig. 4i). Thus, the Phe-BF_3 desilylation system is compatible with nanoparticle-mediated delivery, and shows tumour selectivity.

The pore-forming N-terminal domain (N domain) of gasdermin translocates to the plasma membrane to induce pyroptosis[1–3,5]. The effect of this proinflammatory cell death on tumours is unknown. Our desilylation system provides an ideal approach for investigating this question (Fig. 3a). We used gasdermin A3 (GSDMA3)[19,20], and mutated both cysteine residues in the C-terminal domain (C domain) of gasdermin (thus, conjugation to nanoparticles will occur only via the gasdermin N domain). The mutation did not affect the pyroptosis-inducing activity of the complex formed by the N and C domains of GSDMA3 (GSDMA3(N + C)) (Extended Data Fig. 5a, b). GSDMA3(N + C) was conjugated to 60-nm nanoparticles through the TES ether linker, generating NP–GSDMA3 (Fig. 3a). Upon incubation with Phe-BF_3, GSDMA3(N + C) was released from NP–GSDMA3 and was capable of forming pores on liposome membranes (Extended Data Fig. 5c, d). When HeLa, EMT6 or 4T1 cells, or BMDMs, were treated with NP–GSDMA3 and Phe-BF_3, we observed membrane enrichment of gasdermin N domains (Extended Data Fig. 5e); the cells showed pyroptotic morphology (Fig. 3b). Cells treated with NP–GSDMA3 and Phe-BF_3 released lactate dehydrogenase, which was insensitive to ferroptosis, necroptosis and pan-caspase inhibitors (Extended Data Fig. 5f). Treatment with Phe-BF_3 or NP–GSDMA3 alone caused no pyroptosis. GSDMA3 with E14K and L184D mutations (hereafter, GSDMA3(mut))[19,20], which is deficient in pore-forming, blocked the pyroptosis induced by treatment with NP–GSDMA3 and Phe-BF_3 (Fig. 3b, c, Extended Data Fig. 5g). About 40%, 35% and 20% of HeLa, EMT6 and 4T1 cells, respectively, treated with NP–GSDMA3 and Phe-BF_3 underwent pyroptosis (Fig. 3c). Primary BMDMs died more extensively, owing to their strong phagocytic capacity (Extended Data Fig. 5h).

Similar to NP–[^{89}Zr]GFP, NP–[^{89}Zr]GSDMA3 showed the desired biocompatibility and selective tumour targeting (Extended Data Fig. 6a–d). Transmission electron microscopy confirmed the uptake and cytosolic distribution of NP–GSDMA3 in 4T1 tumours (Extended Data Fig. 6e).

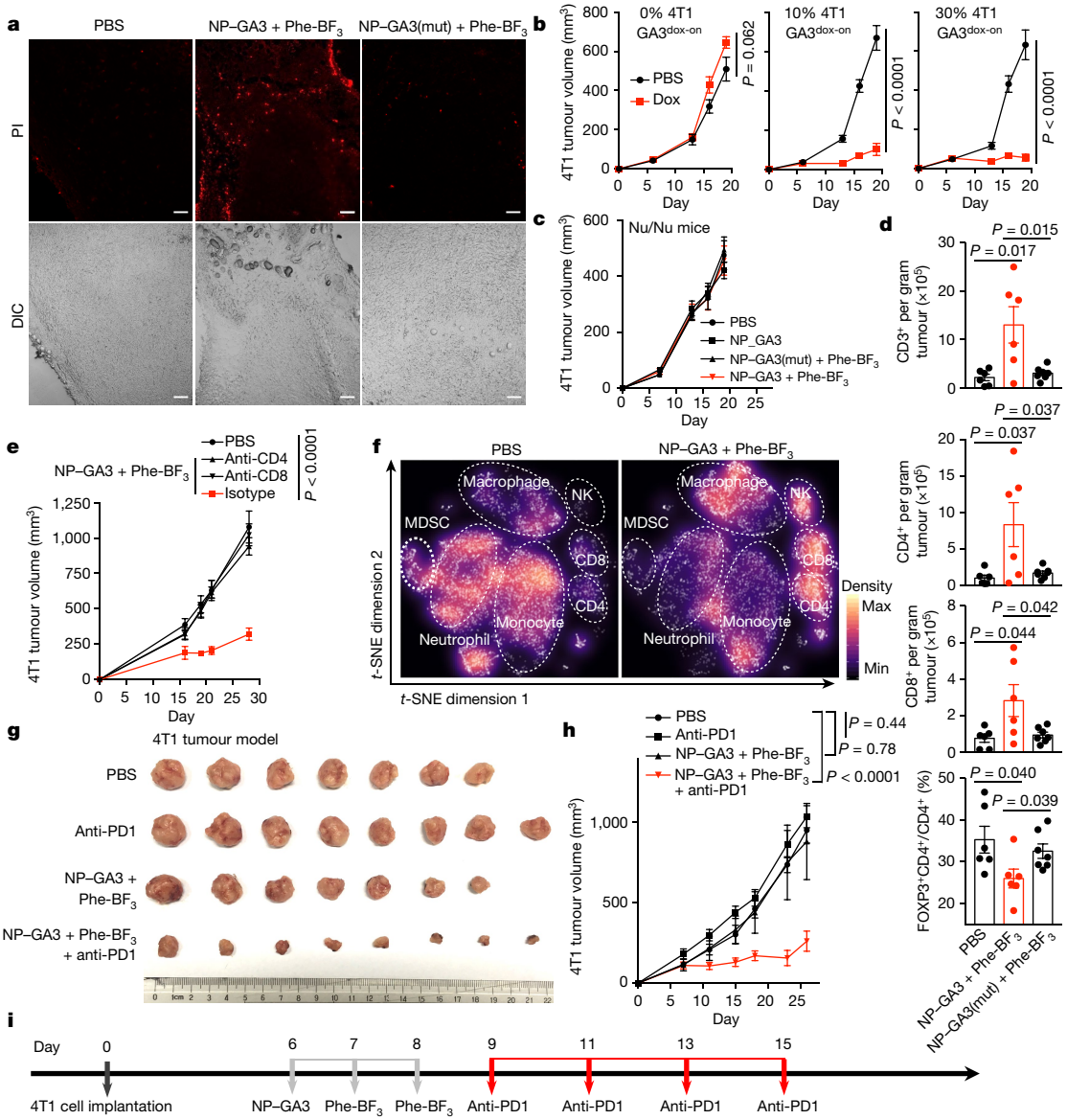

Fig. 5 | A low level of tumour-cell pyroptosis induces effective antitumour immunity and synergizes with anti-PD1 blockade. a, BALB/c mice bearing 4T1 tumours were treated with PBS ($n = 3$), NP–GSDMA3 and Phe-BF_3 ($n = 4$) or NP–GSDMA3(mut) and Phe-BF_3 ($n = 4$), as in Fig. 4b. Propidium iodide was intravenously injected into the mice before assay. Representative tumour-section images are shown. Scale bars, 100 μm. **b**, Normal 4T1 cells mixed with 0%, 10% or 30% 4T1-GSDMA3$^{dox\text{-}on}$ cells were inoculated into BALB/c mice ($n = 7$), followed by intratumoural injection of doxycycline (dox) or PBS on day 6. **c**, Nu/Nu mice bearing 4T1 tumours were treated as in Fig. 4b. $n = 7$ mice for PBS, NP–GSDMA3 and NP–GSDMA3(mut) + Phe-BF_3, 6 mice for NP–GSDMA3 + Phe-BF_3. **d**, Quantification of 4T1-tumour-infiltrating lymphocytes from BALB/c mice. $n = 6$ mice for PBS and NP–GSDMA3 + Phe-BF_3, 7 mice for NP–GSDMA3(mut) + Phe-BF_3. **e**, Anti-CD4 ($n = 9$ mice) or -CD8 ($n = 7$ mice) antibodies or an isotype control ($n = 9$ mice) were intraperitoneally injected into BALB/c mice bearing 4T1 tumours before treatment with NP–GSDMA3 and Phe-BF_3. Mice treated with PBS ($n = 8$) serve as a control. **f**, Single-cell RNA sequencing of CD45$^+$ immune cells from 4T1 tumours treated with PBS or NP–GSDMA3 and Phe-BF_3. *t*-distributed stochastic neighbour embedding (*t*-SNE) density plots of 7,000 CD45$^+$ cells randomly sampled from each group are shown. NK, natural killer. **g**–**i**, Mice bearing 4T1 tumours were treated with PBS ($n = 7$ mice), anti-PD1 ($n = 8$ mice) or NP–GSDMA3 and Phe-BF_3 ($n = 7$ mice) alone, or in combination ($n = 8$ mice). **g**, Photographs of representative tumours at day 26. **h**, Tumour growth curve. **i**, Treatment scheme. In **b**, **c**, **e**, **h**, the average tumour volume at indicated time points is shown. GA3, GSDMA3(N + C). Data shown as mean ± s.e.m. (two-tailed unpaired Student's *t* test) (**b**–**e**, **h**) and representative of two (**a**–**c**, **e**–**h**) and three (**d**) independent experiments.

Thus, distributions of NP–GSDMA3 and Phe-BF_3 also converged onto the tumour (Fig. 4a). The 4T1 cells had no endogenous gasdermin D (GSDMD), gasdermin E (GSDME) and IL-1β (Extended Data Fig. 6f, g). In mice treated with PBS, the volume of 4T1 tumours increased by about 20-fold in 2 weeks (Fig. 4b–d). After three rounds of treatment with NP–GSDMA3 and Phe-BF_3 (Fig. 4b), massive tumour shrinkage occurred and the tumour burden became negligible by day 25 (Fig. 4c, d, Extended Data Fig. 6h, i). The injection of NP–GSDMA3 or Phe-BF_3 alone, or of NP–GSDMA3(mut) and Phe-BF_3, did not cause tumour shrinkage. Tumour weight measurements confirmed the antitumour effect caused by GSDMA3 released from nanoparticles (Fig. 4e). Treatment with NP–GSDMA3 and Phe-BF_3 induced a similar tumour regression in the EMT6 tumour model (Fig. 4f, g). Mice treated with NP–GSDMA3 and Phe-BF_3 showed neither weight loss nor abnormalities in major organs, including the liver and kidneys (Extended Data Fig. 7a, b). Serum concentrations of alkaline phosphatase, calcium and phosphate—as well

as the skeletons—of mice treated with Phe-BF_3 were similar to those of mice treated with PBS (Extended Data Fig. 7c–f).

Intratumoural injection with NP–GSDMA3 and Phe-BF_3 caused the same regression of 4T1 tumours as that caused by intravenous injection (Fig. 4c–e), which suggests that the antitumour effect is the result of GSDMA3 activation at the tumour site. Consistently, mice treated with NP–GSDMA3 and Phe-BF_3 contained a higher number of propidium-iodide-positive pyroptotic cells in the tumour, compared to control mice (Fig. 5a, Extended Data Fig. 6j). Propidium-iodide-positive cells were only a small fraction of the entire tumour-cell population, which is consistent with the 20% pyroptosis that we detected in cultured 4T1 cells (Fig. 3c). Furthermore, we generated 4T1 cells that contain a doxycycline-inducible PreScission protease along with PreScission-protease-cleavable GSDMA3. These cells (which we term 4T1-GSDMA3$^{dox\text{-}on}$ cells) resembled normal 4T1 cells in forming tumour grafts (Fig. 5b). Notably, injecting doxycycline into the tumour completely stopped tumour growth—despite the fact that only 10–30% of 4T1-GSDMA3$^{dox\text{-}on}$ cells were mixed into the inoculated 4T1 cells (Fig. 5b).

The fact that only a fraction of the tumour cells underwent pyroptosis but the entire tumour was eliminated suggests a role of the immune system. Supporting this, athymic Nu/Nu mice (which lack mature T cells) did not show tumour regression after treatment with NP–GSDMA3 and Phe-BF_3 (Fig. 5c). Markedly increased $CD3^+$ T cell infiltration was recorded in tumours treated with NP–GSDMA3 and Phe-BF_3 (Fig. 5d, Extended Data Fig. 8a–c). Both the $CD4^+$ and $CD8^+$ cell populations were increased, whereas the percentage of $CD4^+FOXP3^+$ T regulatory cells decreased; these changes were absent in tumours treated with NP–GSDMA3(mut) and Phe-BF_3 (Fig. 5d, Extended Data Fig. 8a, d, e). Depletion of the $CD4^+$ or $CD8^+$ cell population blocked tumour regression induced by NP–GSDMA3 and Phe-BF_3 (Fig. 5e, Extended Data Fig. 8f). Thus, pyroptosis-induced tumour regression requires both cytotoxic T cells and $CD4^+$ T helper cells.

We performed single-cell RNA sequencing on $CD45^+$ leukocytes from 4T1 tumours of two control and two therapeutically treated mice (Extended Data Fig. 9a). Sequenced cells were clustered into ten immune-cell subsets (Fig. 5f, Extended Data Fig. 9b–d). Compared with tumours treated with PBS, tumours treated with NP–GSDMA3 and Phe-BF_3 had increased $CD4^+$, $CD8^+$ and natural killer cell populations, but decreased monocyte, neutrophil and myeloid-derived suppressor cell populations (Fig. 5f, Extended Data Fig. 9d). The M1 macrophage population also increased whereas the percentage of M2 marker (*Arg1*)-positive cells decreased (Fig. 5f, Extended Data Fig. 9e). Genes that encode chemotactic cytokines (*Ccl5*, *Cxcl9* and *Cxcl10*) or are important for lymphocyte activation (*Cd69* and *Klrk1*) were upregulated in tumours treated with NP–GSDMA3 and Phe-BF_3 (Extended Data Fig. 9f, g). Antitumour effector genes (*Ifng*, *Gzma*, *Gzmb*, *Gzmk* and *Fasl*) were also upregulated, whereas the protumoural or immunosuppressive genes *Csf1*, *Vegfa*, *Arg1*, *Cd274* (which encodes PD-L1) and *Pdcd1lg2* (which encodes PD-L2) were downregulated, in tumours treated with NP–GSDMA3 and Phe-BF_3 (Extended Data Fig. 9e, g). These immunological changes corroborate the potent antitumour effect of injections of NP–GSDMA3 and Phe-BF_3.

IL-1β has an established function in T-cell-mediated antitumour immunity[21,22]. Levels of IL-1β, as well as IL-18, in the serum and the tumour were increased in mice injected with NP–GSDMA3 and Phe-BF_3 (Extended Data Fig. 10a). As expected, levels of HMGB1 also increased. An injection of anti-IL-1β antibody into the tumour-bearing mice severely inhibited the tumour regression induced by treatment with NP–GSDMA3 and Phe-BF_3, whereas anti-IL-18 and anti-HMGB1 antibodies showed partial and no effects, respectively (Extended Data Fig. 10b). Thus, IL-1β—probably derived from activated macrophages—is required for antitumour immunity induced by pyroptosis of tumour cells. Immune checkpoint blockade (particularly using anti-PD1) is highly successful in the treatment of cancer, but has a low response rate[23,24]. One main cause of this low response rate is that inflammation within the tumour microenvironment is low or ineffective for sufficient infiltration and/or activation of T lymphocytes; thus, the tumours resistant to checkpoint blockade are deemed to be 'cold'[25]. The 4T1 tumour—which is known to be cold—did not respond to anti-PD1 treatment (Fig. 5g, h). One round of injection with NP–GSDMA3 and Phe-BF_3 also did not prevent tumour growth (Fig. 5g, h). Notably, when the one-round injection was followed by anti-PD1 treatment (Fig. 5i), a marked shrinkage in tumour volume and reduction in tumour weight occurred (Fig. 5g, h, Extended Data Fig. 10c). Thus, pyroptosis-induced inflammation within the tumour microenvironment can synergize with checkpoint blockade in inducing antitumour immunity.

Here we show that the Phe-BF_3 desilylation bioorthogonal system operates efficiently in the animal, which potentially can be combined with other methods for new applications. The application of our system to gasdermin activation uncovers an antitumour immune effect of pyroptosis. Thus, a gasdermin agonist may improve the efficacy of cancer immunotherapy. An immune-dependent anticancer effect has long been known for cell-killing chemotherapeutic drugs[26,27]; this effect might be due to gasdermin activation. Direct gasdermin activation, via desilylation mediated by Phe-BF_3, provides a powerful system for developing mechanistic understandings of the antitumour immunity stimulated by immunogenic cell death such as pyroptosis.

Online content

Any methods, additional references, Nature Research reporting summaries, source data, extended data, supplementary information, acknowledgements, peer review information; details of author contributions and competing interests; and statements of data and code availability are available at https://doi.org/10.1038/s41586-020-2079-1.

1. Kayagaki, N. et al. Caspase-11 cleaves gasdermin D for non-canonical inflammasome signalling. *Nature* **526**, 666–671 (2015).
2. Shi, J. et al. Cleavage of GSDMD by inflammatory caspases determines pyroptotic cell death. *Nature* **526**, 660–665 (2015).
3. Shi, J., Gao, W. & Shao, F. Pyroptosis: gasdermin-mediated programmed necrotic cell death. *Trends Biochem. Sci.* **42**, 245–254 (2017).
4. Wang, Y. et al. Chemotherapy drugs induce pyroptosis through caspase-3 cleavage of a gasdermin. *Nature* **547**, 99–103 (2017).
5. Broz, P., Pelegrín, P. & Shao, F. The gasdermins, a protein family executing cell death and inflammation. *Nat. Rev. Immunol*. https://doi.org/10.1038/s41577-019-0228-2 (2019).
6. Liu, Z. et al. Preclinical evaluation of a high-affinity ^{18}F-trifluoroborate octreotate derivative for somatostatin receptor imaging. *J. Nucl. Med.* **55**, 1499–1505 (2014).
7. Liu, Z. et al. Boramino acid as a marker for amino acid transporters. *Sci. Adv.* **1**, e1500694 (2015).
8. Liu, Z. et al. An organotrifluoroborate for broadly applicable one-step ^{18}F-labeling. *Angew. Chem. Int. Edn Engl.* **53**, 11876–11880 (2014).
9. David Crouch, R. Selective monodeprotection of bis-silyl ethers. *Tetrahedron* **60**, 5833–5871 (2004).
10. Chau, C. H., Steeg, P. S. & Figg, W. D. Antibody–drug conjugates for cancer. *Lancet* **394**, 793–804 (2019).
11. Perrin, D. M. [^{18}F]-Organotrifluoroborates as radioprosthetic groups for PET imaging: from design principles to preclinical applications. *Acc. Chem. Res.* **49**, 1333–1343 (2016).
12. Nelson, T. D. & Crouch, R. D. Selective deprotection of silyl ethers. *Synthesis* **1996**, 1031–1069 (1996).
13. Handy, C. J., Lam, Y. F. & DeShong, P. On the synthesis and NMR analysis of tetrabutylammonium triphenyldifluorosilicate. *J. Org. Chem.* **65**, 3542–3543 (2000).
14. Liu, Z. et al. From minutes to years: predicting organotrifluoroborate solvolysis rates. *Chemistry* **21**, 3924–3928 (2015).
15. Papasani, M. R., Wang, G. & Hill, R. A. Gold nanoparticles: the importance of physiological principles to devise strategies for targeted drug delivery. *Nanomedicine* **8**, 804–814 (2012).
16. Wilhelm, S. et al. Analysis of nanoparticle delivery to tumours. *Nat. Rev. Mater.* **1**, 16014 (2016).
17. Blanco, E., Shen, H. & Ferrari, M. Principles of nanoparticle design for overcoming biological barriers to drug delivery. *Nat. Biotechnol.* **33**, 941–951 (2015).
18. Swierczewska, M., Lee, S. & Chen, X. The design and application of fluorophore–gold nanoparticle activatable probes. *Phys. Chem. Chem. Phys.* **13**, 9929–9941 (2011).
19. Ding, J. et al. Pore-forming activity and structural autoinhibition of the gasdermin family. *Nature* **535**, 111–116 (2016).
20. Ruan, J., Xia, S., Liu, X., Lieberman, J. & Wu, H. Cryo-EM structure of the gasdermin A3 membrane pore. *Nature* **557**, 62–67 (2018).
21. Ghiringhelli, F. et al. Activation of the NLRP3 inflammasome in dendritic cells induces IL-1β-dependent adaptive immunity against tumors. *Nat. Med.* **15**, 1170–1178 (2009).

22. Lee, P. H. et al. Host conditioning with IL-1β improves the antitumor function of adoptively transferred T cells. *J. Exp. Med*. **216**, 2619–2634 (2019).
23. Zou, W., Wolchok, J. D. & Chen, L. PD-L1 (B7-H1) and PD-1 pathway blockade for cancer therapy: mechanisms, response biomarkers, and combinations. *Sci. Transl. Med*. **8**, 328rv4 (2016).
24. Ribas, A. & Wolchok, J. D. Cancer immunotherapy using checkpoint blockade. *Science* **359**, 1350–1355 (2018).
25. Sharma, P. & Allison, J. P. The future of immune checkpoint therapy. *Science* **348**, 56–61 (2015).
26. Schwartz, H. S. & Grindey, G. B. Adriamycin and daunorubicin: a comparison of antitumor activities and tissue uptake in mice following immunosuppression. *Cancer Res*. **33**, 1837–1844 (1973).
27. Casares, N. et al. Caspase-dependent immunogenicity of doxorubicin-induced tumor cell death. *J. Exp. Med*. **202**, 1691–1701 (2005).

Methods

No statistical methods were used to predetermine sample size. The experiments were not randomized and investigators were not blinded to allocation during experiments and outcome assessment.

Chemical reagents, plasmids and antibodies

5-Fluorouracil (5-FU) (920052), leflunomide (448506), capecitabine (392078) and fluorodeoxyglucose (D234500) were obtained from J&K Scientific. Synthesis and characterization of compounds 1 to 6 (Extended Data Fig. 1c, d) are described and shown in the Supplementary Methods, Supplementary Figs. 2–27. Other chemical reagents and solvents used in this study were purchased from Sigma-Aldrich, J&K Scientific, Energy Chemical or Thermo Fisher Scientific. All nuclear magnetic resonance (NMR) spectra were recorded at room temperature on a Bruker Avance 400-MHz or 600-MHz spectrometer. Signals are presented as ppm, and multiplicity is identified as single (s), broad (br), doublet (t), triplet (t), quartet (q) or multiplet (m); coupling constants are in Hz. The concentration of the compounds was performed by rotary evaporation without heating at an appropriate reduced pressure. Chemistry yields refer to the isolated pure chemicals.

Complementary DNA (cDNA) for mouse *Gsdma3* was synthesized by our in-house gene-synthesis facility. cDNA for *eGFP* and *mNeonGreen* were gifts from P. Xu. The cDNA was cloned into a modified pET vector with an N-terminal 6×His-SUMO tag for recombinant expression in *Escherichia coli*. cDNA for *mNeonGreen-NLS* was generated by standard PCR cloning strategy, with a reverse primer containing the SV40 NLS sequence (5′-CCGAAAAAACGTAAAGTT-3′). The cDNA was inserted into a modified pCS2-3×Flag vector for transient expression in HeLa cells. Primers used for generating point mutations were designed using an online program (https://www.agilent.com/store/primerDesignProgram.jsp). All plasmids were verified by DNA sequencing.

For fluorescence-activated cell sorting (FACS) analyses of tumour-infiltrating lymphocytes, PE-conjugated anti-mouse CD3 (clone 17A2), FITC-conjugated anti-mouse CD4 (clone RM4.5) and APC-conjugated anti-mouse CD8 (clone 53-6.7) were purchased from BioLegend. eFluor-450-conjugated anti-mouse FOXP3 antibody (clone FJK-16s) was obtained from Invitrogen. The trastuzumab used to generate the antibody–drug conjugate was a gift from the Beijing People's Hospital. The PD1 antibody used for treating 4T1 tumours was a gift from BeiGene. For immune-cell depletion, anti-mouse CD4 (clone GK1.5) and isotype control (clone LTF-2) antibodies were produced by BioXcell, and anti-mouse CD8 was a gift from J. Sui. Anti-LAT1 antibody (D-10) was obtained from Santa Cruz Biotechnology. Anti-GFP (11814460001) and anti-Na, K-ATPase α1(2047-1) were obtained from Roche and Epitomics, respectively. Anti-GAPDH and anti-Flag antibodies were purchased from Sigma-Aldrich. Anti-GSDME (ab215191) and anti-GSDMD (ab219800) were from Abcam. Anti-IL-1β (GTX74034) was obtained from Genetex.

Synthesis and isolation of TESO–coumarin, TBSO–coumarin- and TIPSO–coumarin

The synthetic routes for TESO–coumarin, TBSO–courmarin and TIPSO–coumarin are essentially the same, and are illustrated in Extended Data Fig. 1c. In brief, coumarin–NCO (500 mg, 2.48 mmol) was dissolved in dry THF (15 ml), and then mixed with compound 5 (1.0 equivalent, 2.37 mmol) and dibutyltin dilaurate (DBTL, 0.05 equivalent, 0.12 mmol) under N_2 atmosphere. The solution was stirred under refluxing THF for 24 h. Without washing, the organic layer was removed under reduced pressure. The residue was purified by flash chromatography to obtain silyl-ether-conjugated coumarin as the white solid (40% yield). TESO–coumarin: ^{1}H NMR (600 MHz, DMSO-d_6) δ 7.75–7.65 (m, 2H), 7.62–7.51 (m, 2H), 7.44 (dt, J = 8.8, 2.6 Hz, 1H), 6.85 (dd, J = 8.5, 3.9 Hz, 1H), 6.24 (s, 1H), 5.14 (d, J = 15.1 Hz, 2H), 2.48–2.30 (m, 9H), 0.92 (dt, J = 25.9, 7.8 Hz, 9H), 0.75 (q, J = 8.0 Hz, 3H) (Supplementary Fig. 2). TBSO–coumarin: ^{1}H NMR (400 MHz, DMSO-d_6) δ 10.51 (s, 1H), 10.31 (s, 1H), 7.73–7.64 (m, 2H), 7.56 (d, J = 1.9 Hz, 2H), 7.43 (dd, J = 8.6, 1.9 Hz, 1H), 6.88 (d, J = 8.7 Hz, 1H), 6.24 (s, 1H), 5.13 (s, 2H), 3.74 (s, 2H), 3.35 (s, 6H), 2.38 (s, 3H), 0.95 (s, 9H), 0.23 (s, 6H). ^{13}C NMR (101 MHz, DMSO) δ 160.06, 153.83, 153.23, 153.22, 149.51, 142.79, 131.89, 126.32, 126.06, 121.74, 121.23, 118.67, 114.38, 114.30, 111.91, 104.46, 61.98, 45.26, 43.96, 25.53, 18.02, 17.88, 8.41, −4.44 (Supplementary Fig. 3). TIPSO–coumarin: ^{1}H NMR (400 MHz, DMSO-d_6) δ 10.28 (s, 1H), 7.70 (d, J = 8.7 Hz, 1H), 7.64 (d, J = 1.9 Hz, 1H), 7.57–7.49 (m, 2H), 7.43 (dd, J = 8.7, 1.8 Hz, 1H), 6.86 (d, J = 8.8 Hz, 1H), 6.27–6.20 (m, 1H), 5.19 (s, 2H), 2.55 (s, 5H), 2.41–2.37 (m, 3H), 1.07 (d, J = 1.3 Hz, 16H), 1.04 (s, 3H) (Supplementary Fig. 4). High-performance liquid chromatography (HPLC)–mass spectrometry was used to analyse the stability of the synthesized TESO–coumarin, TBSO–coumarin and TIPSO–coumarin (Supplementary Figs. 22–24).

Synthesis and isolation of the TESO–linker (compound 7) and the TBSO–linker (compound 7′) for NP conjugation

Compound 6 (1.0 equivalent, 1 mmol) and DBTL (0.05 equivalent, 0.05 mmol) were dissolved in acetone (10 ml) under N_2 atmosphere. The solution was stirred under refluxing THF for 48 h. Without washing, the organic layer was removed under reduced pressure. The residue was purified by flash chromatography to obtain compound 7. This synthetic route is shown in Extended Data Fig. 1d. ^{1}H NMR (400 MHz, chloroform-d) δ 7.75–7.68 (m, 1H), 7.53 (dd, J = 5.6, 3.3 Hz, 2H), 7.35 (s, 1H), 6.74 (d, J = 8.6 Hz, 1H), 5.08 (s, 2H), 3.81 (d, J = 6.0 Hz, 2H), 3.57 (s, 2H), 3.46–3.38 (m, 3H), 3.21 (q, J = 4.8, 3.5 Hz, 2H), 2.67 (s, 6H), 1.71 (dd, J = 14.7, 6.8 Hz, 2H), 1.43 (t, J = 7.2 Hz, 3H), 0.98 (t, J = 7.9 Hz, 11H), 0.76 (q, J = 7.9 Hz, 8H) (Supplementary Fig. 9). HPLC and high-resolution mass spectrometry were used to analyse the quality of the synthesized TESO–linker (Supplementary Figs. 25, 27).

TBSO–linker (compound 7′) ^{1}H NMR (600 MHz, DMSO-d_6) δ 7.51–7.50 (m, 1H), 7.29–7.25 (m, 1H), 6.81–6.79 (m, 1H), 6.66 (s, 2H), 4.92 (s, 1H), 4.45 (s, 2H), 3.74–3.72 (t, 2H), 3.44–3.41 (m, 2H), 3.17–3.11 (t, 2H), 2.45–2.33 (s, 6H), 2.03–1.95 (m, 2H), 1.88–1.71 (m, 4H), 0.97 (s, 9H), 0.20 (s, 6H) (Supplementary Fig. 10).

Chromatography analysis to determine the efficiency of the desilylation reaction

TESO–coumarin, TBSO–coumarin and TIPSO–coumarin (150 μM) were treated with Phe-BF_3 (150 μM) in PBS (including 5% DMSO) at 37 °C. HPLC analysis was performed at 5 and 240 min after incubation (Extended Data Fig. 3d, e). For bioorthogonality evaluation (Extended Data Fig. 3f), TESO–coumarin (150 μM) was treated with H_2O_2, GSH or other biologically relevant anions, including Cl^-, I^-, NO_3^-, PO_4^{3-} and SO_4^{2-} (150 μM) in PBS (including 5% DMSO) at 37 °C. HPLC analysis was performed at 240 min after incubation. To compare the reaction efficiency of Phe-BF_3 with those of other fluorine donors (Extended Data Fig. 3g), TESO–coumarin (150 μM) was treated with Phe-BF_3 or another organofluorines in PBS (including 5% DMSO) at 37 °C. HPLC analysis was performed at 240 min after incubation. An Agilent Eclipse XDB-C18 5-μm, 4.6 × 250-mm analytical column was used for the HPLC analyses, and leflunomide (c = 20 μM) was added as the internal standard. Solvent A was water (0.1% TFA); solvent B was MeCN; 0 to 2 min: 5% B, 2 to 10 min: 5% to 95% B, 10 to 15 min: 95% B, 15 to 17 min: 95% to 5% B; flow rate: 0.6 ml/min; column temperature: 19 to 21 °C. The reaction yields were determined by HPLC peak integration at the given wavelength (254 nm) (Supplementary Figs. 16–21). In addition, the desilylation rate constant was determined by liquid chromatography analysis as previously described[28]. All the measurements were performed in triplicate and the average numbers are shown.

Evaluation of MMAE release efficiency in vitro and in vivo

To evaluate the desilylation efficiency in vitro, trastuzumab–SEC–MMAE stock solution (100 nM, 3 ml) and Phe-BF_3 stock solution (20 μM, 3 ml) were mixed and incubated at 37 °C in PBS for 3 h, 15 h, 20 h or

24 h. One hundred microlitres of acetonitrile was added to the crude product to remove the protein, and the crude product was then centrifuged at 10,000 rpm for 3 min. Ten microlitres of the supernatant was analysed, and the content of MMAE released was measured by liquid chromatography–mass spectrometry analysis. A Hypersil GOLD 1.9-μm 2.1 × 100-mm analytical column was used for the HPLC analyses. Solvent A was water (0.1% FA); solvent B was MeCN; 0 to 2 min: 5% B, 2 to 10 min: 5% to 95% B, 10 to 14 min: 95% B, 14 to 15 min: 95% to 5% B, 15 to 17 min: 5% B; flow rate: 0.3 ml/min; column temperature: 19 to 21 °C. The reaction yields were determined by HPLC peak integration at the given mass spectrum signal. All the measurements were performed in triplicate and the average numbers are shown. To evaluate the desilylation efficiency in vivo, the tumour-bearing mice that had been intravenously injected with trastuzumab–SEC–MMAE were divided into two groups, which were left untreated or treated with Phe-BF_3 every two days. The tumours were collected on the fifth day ($n = 4$), frozen with liquid nitrogen, ground into powder and then extracted by methanol. After removing the methanol by rota-evaporation, the precipitates were redissolved in PBS, in which MMAE was quantified by methods described in previous publications[29,30].

Preparation and characterization of trastuzumab–SEC–MMAE

Trastuzumab in 4.8 ml of PBS (10 mg/ml) was treated with tris(2-carboxyethyl)phosphine (2.3 equivalents) at 37 °C for 30 min to make the reduction reaction was complete. The reaction crude product was diluted with PBS until the antibody concentration was 2.5 mg/ml, and cooled to 4 °C. The reduced antibody was then reacted with maleimide–SEC–MMAE (about 8.0 equivalents) in dimethyl sulfoxide stock solution for 1 h on ice. The conjugation reaction was quenched by a 20-fold excess of cysteine over maleimide. The reaction crude products were concentrated by centrifugal ultrafiltration and the trastuzumab–SEC–MMAE conjugation product was purified by elution through a PD10 column in PBS and then stored at −80 °C for analyses and experiments. The drug-to-antibody ratio was determined by UV–visible spectrum and matrix-assisted laser desorption/ionization time-of-flight (MALDI TOF) mass spectrometry as previously described[31].

Radiochemistry and PET imaging

[^{18}F]Phe-BF_3 was radiosynthesized via the one-step ^{18}F–^{19}F isotope exchange (IEX) reaction. The labelling method and purification procedure have previously been described[7,32]. PET scans were obtained, and image analysis was performed, using a Mediso 122 s PET scanner. About 3.7 MBq of [^{18}F]Phe-BF_3, ^{89}Zr-labelled antibody–drug conjugates and ^{89}Zr-labelled protein–nanoparticle conjugates were administered via tail-vein injection under isoflurane anaesthesia. Standard data acquisition and image reconstruction of the PET data were performed.

Preparation of DBCO–PEG-decorated nanoparticles

The water-soluble spherical gold nanoparticles (A68095) were generated by 3A Chemicals. PEG-decorated nanoparticles were prepared according to published methods[33,34]. In brief, a solution of nanoparticles (60 nm) containing citric acid was centrifuged at 14,000*g* for 5 min, decanted and resuspended in water to remove excess citric acid. Ten microlitres of 10 mM DBCO–PEG3400–SH were added to 1 ml of 0.2 mg/ml nanoparticle solution. The mixture was stirred for 30 min at room temperature, and 40 μl of 10 mM MeO–PEG5000–SH were then added, stirring for 24 h at 4 °C. The reaction crude products were centrifuged at 14,000*g* for 5 min, decanted and resuspended in water to remove excess PEG. The size of the DBCO–PEG-decorated nanoparticles (DBCO–PEG–NPs) was confirmed by transmission electron microscopy (Supplementary Fig. 28).

Preparation of NP–GFP, NP–mNeonGreen–NLS and NP–GSDMA3 materials

The desired nanoparticle–protein conjugates were prepared following previous publications[35,36]. In brief, to obtain NP–GFP and NP–mNeonGreen–NLS, 100 μl of N_3–OTES–maleimide linker (compound 7, TESO–linker) (PBS, 500 μM) was added to 100 μ; of GFP or mNeonGreen–NLS solution (PBS, 100 μM) at 4 °C for 24 h. Excess linker was removed from the solution by ultrafiltration centrifugation 4 times, and the modified GFP or mNeonGreen–NLS protein was obtained. One hundred microlitres of each of the modified proteins (20 μM) was reacted with 100 μl of DBCO–PEG–NP solution (0.2 mg/ml) with stirring at room temperature for 30 min. After overnight storage at 4 °C, the reaction was centrifuged at 5,000*g* for 5 min, decanted and resuspended in water to remove excess unconjugated proteins. To prepare NP–GSDMA3, all operations were carried out at 4 °C. One hundred microlitres of N_3–OTES–maleimide linker (PBS, 500 μM) was added slowly to 100 μl of the GSDMA3(N+C) nonvalent complex (60 μM) solution, and the reaction proceeded for 6 h. Excess linker was removed by overnight dialysis. After centrifugation to remove the precipitate, the modified GSDMA3 protein was obtained and resuspended in PBS. One hundred microlitres of the modified GSDMA3 protein (20 μM) was incubated with 100 μl of DBCO–PEG–NP solution (0.2 mg/ml) for 6 h. The mixture was used directly to treat cells or mice.

Transmission electron microscopy and negative-staining electron microscopy

4T1 cells (1×10^6) were implanted into the right flank of BALB/c female mice (6–8 weeks old). Mice were intravenously injected with NP–GSDMA3 on day 6. The 4T1 tumours (about 100 mm^3) were collected on day 8. The freshly isolated tumours were minced into tissue blocks (about 2 mm^3) and fixed with 2% paraformaldehyde and 2% glutaraldehyde immediately, followed by secondary fixing with 1% OsO_4 and en bloc staining with 2% uranyl acetate. Samples were then dehydrated through a progressive lowering of temperature method (an ascending acetone series 15–100% in 7 steps). The samples were then embedded in SPI-PON 812 resin (Sigma-Aldrich) and sectioned to 90 nm. The ultrathin sections were stained with 3% uranyl acetate for 7 min and Sato's lead for 2 min before imaging on a 120-kV Tecnai G2 Spirit electron microscope (FEI). Reconstitution and imaging of the GSDMA3 pore by negative-staining electron microscopy were performed following the same protocol as previously described[20].

Side-effect analysis in mouse tumour model

For the histological assessment in Extended Data Fig. 7b, tumour-bearing mice were killed after the indicated treatments, and the kidney and the liver were removed and fixed overnight with 4% formalin. After dehydration by gradient ethanol treatment, the tissue samples were embedded in paraffin and sectioned for haematoxylin and eosin staining. Independent experiments were performed with three mice for each experimental group. Blood samples of mice treated with Phe-BF_3 or PBS were also collected for serum isolation. The serum levels of alkaline phosphatase (P0321, Beyotime), calcium (S1063S, Beyotime) and phosphate (DIPI007, BioAssay Systems) were determined following the manufacturers' instructions.

Cell culture and transfection

HeLa, EMT6 and CT26 cells were obtained from the American Type Culture Collection. The 4T1 cells were obtained from the China Infrastructure of Cell Line Resources. Primary BMDMs were prepared and cultured by following a standard protocol, as previously described[2]. The cells were frequently checked by their morphological features and functionalities, but were been subjected to authentication by short tandem repeat profiling. All cell lines were tested for mycoplasma regularly, using the commonly used PCR strategy. The 4T1, EMT6 and CT26 cells and primary BMDMs were cultured in RIPM 1640 medium and HeLa cells were cultured in Dulbecco's modified Eagle's medium. The media were supplemented with 10% (v/v) fetal bovine serum (FBS) and 2 mM L-glutamine. All cells were cultured in a 5% CO_2 incubator at 37 °C. Transient transfection was performed with the JetPRIME (Polyplus

Transfection) by following the manufacturer's instructions. Full-length GSDMA3 or GSDMA3(N + C) proteins were electroporated into CT26 cells using the Neon Transfection System (Life Technologies).

Immunostaining and fluorescence microscopy

Frozen 4T1 tumour sections were used for anti-CD3 immunostaining. At the end of indicated treatments on day 16, 4T1 tumours were dissected from mice and embedded into Cryomold moulds filled with the OCT compound (SAKURA 4583). The tissue samples were frozen on dry ice for 30 min and stored at −20 °C. For immunostaining, the frozen tumour tissues were sectioned into 10-μm pieces using cryostat (Lecia CM1950) and mounted on slides. After washing out the OCT with PBS, the slices were fixed with 4% paraformaldehyde for 30 min and then blocked and permeabilized with PBS containing 1% FBS and 0.2% Triton X-100 for 1 h. The slides were stained with PE-conjugated anti-mouse CD3 antibody for 1 h and Hoechst for 1 min. Zeiss LSM800 confocal laser scanning microscope was used to acquire images on the 10× or 40× objectives.

The 4T1 tumour model was used for quantifying Phe-BF_3-mediated release of mNeonGreen–NLS from NP–mNeonGreen–NLS. The NP–mNeonGreen–NLS conjugates were administered into 4T1 tumour-bearing mice through intravenous injections on day 6, 9 and 12 followed by intravenous injections of Phe-BF_3 on day 7, 8, 10, 11, 13 and 14. On day 15, mice were killed and tumours were dissected from the surrounding fascia, embedded in the Cryomold moulds filled with the OCT compound and frozen. Processing of the tumour tissue was performed as described for anti-CD3 staining and the slides were stained with Alexa-Fluor-647-conjugated phalloidin (A22287, Thermo Fisher Scientific). Zeiss LSM850 confocal microscope was used to record the images on a 60× oil objective.

Pyroptosis assays

HeLa, EMT6 and 4T1 cells, and primary BMDMs, were seeded into a 6- or 96-well plate 24 h before being subjected to the indicated treatments. To examine cell morphology, annexin V–FITC and propidium iodide were added to the cell-culture medium before subjected to imaging on an LSM800 confocal microscope. To examine cell morphology, static bright-field images of pyroptotic cells were captured using an Olympus IX71 microscope. The image data shown are representative of at least three randomly selected fields. For flow cytometry analysis, all cells in each 6-well plate were collected and washed twice with PBS, stained by using the annexin V–FITC and PI staining kit (Abmaking) (annexin V–FITC for 10 min and propidium iodide for 5 min). The sample volume was increased to 500 μl by adding more PBS, and the samples were analysed on a BD FACS Aria III flow cytometer. Data were processed using FlowJo software. Cell viability and LDH release assays were determined by using the CellTiter-Glo Luminescent Cell Viability Assay (Promega) and LDH-Glo Cytotoxicity Assay (Promega), respectively. A membrane protein isolation kit (SM-005, Invent Biotechnologies) was used to detect the translocation of the GSDMA3 N domain to the cell membrane.

Purification of recombinant proteins

To obtain engineered GSDMA3 protein containing the PreScission protease (PPase) cleavage site and the mNeonGreen–NLS proteins, *E. coli* BL21 (DE3) cells containing pET28a-6×His-SUMO-GSDMA3 or mNeonGreen–NLS were grown in Luria–Bertani (LB) medium supplemented with 30 μg/ml kanamycin. After the optical density at 600 nm of the culture reached 0.8, 0.4 mM isopropyl-B-D-thiogalactopyranoside (IPTG) was added to induce protein expression at 18 °C overnight. Bacteria were collected and sonicated in the lysis buffer containing 20 mM Tris-HCl (pH 8.0), 150 mM NaCl, 20 mM imidazole and 10 mM 2-mercaptoethanol. The fusion protein was first affinity-purified by Ni-Sepharose beads (GE Healthcare Life Sciences). The homemade ULP1 protease was used to remove the 6×His–SUMO tag by overnight cleavage at 4 °C. HiTrap Q ion-exchange and Superdex G75 gel-filtration chromatography (GE Healthcare Life Sciences) were then performed sequentially for further purification. To obtain the GSDMA3(N + C) noncovalent complex, the purified engineered GSDMA3 protein was digested overnight with homemade PPase at 4 °C. The GSDMA3(N + C) complex was further purified by Superdex G75 gel-filtration chromatography in the absence of reductants. 2-Mercaptoethanol present in the mNeonGreen–NLS protein was also removed at Superdex G75 gel-filtration chromatography step.

Stimulation of cells with nanoparticle–protein conjugates and Phe-BF_3

HeLa, EMT6 and 4T1 cells, and primary BMDMs, seeded in 6-well plates were treated with the NP–GSDMA3 conjugates for 24 h. Subsequently, the medium containing NP–GSDMA3 was replaced with medium containing Phe-BF_3, and incubated for another 24 h. The cells were then subjected to flow cytometry analyses. For confocal microscopy imaging assay of GFP release from NP–GFP, primary BMDMs were seeded onto glass coverslips in 24-well plates and treated sequentially with the NP–GFP conjugate for 24 h and Phe-BF_3 for another 24 h. The treated cells were washed with PBS and fixed with 4% paraformaldehyde. The nucleus was stained with Hoechst. Fluorescence images were captured by using the Zeiss LSM800 confocal microscope on a 20× objective.

In vivo propidium iodide staining assay of tumour cell pyroptosis

For propidium iodide labelling of pyroptotic cells in vivo, mice bearing 4T1 tumours were administered propidium iodide (2.5 mg/kg) via intravenous injection at 24 h after the last round of treatment with NP–GSDMA3 and Phe-BF_3 (Fig. 4b). Ten minutes later, the mice were killed and the tumours were collected, placed into OCT-containing Cryomold moulds and frozen. After slicing and mounting, the slides were scanned directly and immediately on the Zeiss LSM800 confocal microscope.

Tumour model and FACS analyses of tumour-infiltrating lymphocytes

All mice used were purchased from the Vital River Laboratories. To construct the tumour model, BGC823 (1×10^6), 4T1 (1×10^6) or EMT6 (2×10^6) cells in 100 μl of PBS were implanted into the right flank of Nu/Nu nude female mice (for BGC823 cells) or BALB/c female mice (6–8 weeks old). Mice were intravenously injected with NP–GSDMA3 or an indicated control on day 6, 9 and 12, and each of the 3treatments was followed by 2 intravenous injections of Phe-BF_3 (on day 7, 8, 10, 11, 13 and 14), as illustrated in Fig. 4b. For the doxycycline tumour model in Fig. 5b, normal 4T1 cells mixed with 0%, 10% or 30% 4T1-GSDMA3$^{dox\text{-}on}$ cells (total cell number of 1.5×10^6) were implanted into the right flank of BALB/c female mice (6–8 weeks old). Doxycycline (20 μg for each mouse) or PBS were intratumourally injected into the mice at day 6. For the combinatory therapy in Fig. 5g–i, anti-PD1 antibody (5 mg/kg) was intraperitoneally injected into the mice on day 9, 11, 13 and 15 after a single round of treatment with NP–GSDMA3 and Phe-BF_3 from day 6 to day 8. When the tumour was palpable, its long diameter (L) and short diameter (W) were measured every 3–5 days with a calliper; the tumour volume was determined using the volume formula for an ellipsoid (that is, $1/2 \times L \times W^2$). Mice were killed by CO_2 inhalation when the tumour reached 2,000 mm^3. The same protocol was used to construct the 4T1 tumour model in the Nu/Nu mice. For FACS of tumour-infiltrating lymphocytes, tumours were collected on day 16 after inoculation. The tumours were dissected from the surrounding fascia, weighted, minced into pieces by sterile scissors and ground. Cell clumps were removed through a 70-μm cell strainer to obtain single-cell suspensions. The suspension was centrifuged and the cell pellets were washed twice with PBS containing 1% BSA (FACS buffer). Lymphocytes were isolated by Percoll density-gradient centrifugation, washed and resuspended in the FACS buffer, blocked with anti-mouse CD16/CD32 (clone 93, BioLegend) for 30 min, and finally stained with the indicated

antibodies for another 1 h. The LIVE/DEAD Fixable Near-IR Dead Cell Stain Kit (L10119, Invitrogen) was used to determine cell viability during FACS analysis. The FOXP3 Fixation/Permeabilization Kit (00-5521-00, Invitrogen) was used to stain the intracellular FOXP3, following the manufacturer's instructions.

Single-cell RNA sequencing

The tumour-infiltrating lymphocytes isolated as in 'Tumour model and FACS analyses of tumour-infiltrating lymphocytes' were stained with PE-conjugated anti-mouse CD45 antibody (clone 30-F11, Biolegend). $CD45^+$ immune cells were then enriched by using a BD FACS Aria III flow cytometer. Cell viability was monitored in real time during preparation of the single $CD45^+$ immune-cell suspension. Ten thousand cells (about 600 single cells per microlitre) from each experimental group were barcoded and pooled using the 10x Genomics device. Samples were prepared following the manufacturer's protocol and sequenced on an Illumina NextSeq sequencer. The Cell Ranger analysis pipeline (v.3.0.2) was used for sample demultiplexing, barcode processing, alignment, filtering, UMI counting and aggregation of the sequencing runs. For quality control of the single-cell RNA-sequencing procedure, cells with less than 300 genes detected —as well as cells with transcript counts for mitochondria-encoded genes of more than 15% of the total transcript counts—were removed from subsequent analyses. Genes detected in fewer than three cells across the dataset were also excluded, yielding a preliminary expression matrix of 18,069 cells. After obtaining the digital gene-expression data matrix, Seurat (v.3.0.0.9000) was used for dimension reduction, clustering and differential gene-expression analyses.

Immune-cell depletion and cytokine neutralization

Each tumour-bearing mouse was intraperitoneally administered 200 μg of anti-mouse CD4, anti-mouse CD8 or the isotype-control antibody on day 5, 8, 11 and 14 after inoculation of the 4T1 cells. To verify the depletion efficiency, the percentage of $CD4^+$ or $CD8^+$ T lymphocytes in the spleen was determined on day 16 by using a BD FACSAria III flow cytometer. For cytokine neutralization experiments, 100 μg of anti-IL-1β (BE0246, BioXcell) or anti-IL-18 (BE0237, BioXcell) was intraperitoneally injected into each tumour-bearing mouse 3 times (once every 3 days). Two hundred micrograms of anti-HMGB1 (a gift from F. Zheng) was intraperitoneally injected into the mouse five times every two days to neutralize the HMGB1 protein.

Animal ethics and general protocols of animal studies

All mouse studies were conducted in accordance with the principles and procedures outlined in the Guide for the Care and Use of Laboratory Animals (Ministry of Health, China) and the protocol was approved by the Institutional Animal Care and Use Committee (IACUC) of Peking University (IACUC ID: CCME-LiuZB-1). The tumour-bearing mice were subjected to indicated treatments and small-animal PET studies when the tumour volume reached 100 mm^3 (about 1 week after inoculation) and 100–300 mm^3 (2–3 weeks after inoculation), respectively. Ethical compliance with the IACUC protocol was maintained. In none of the experiments did the size of tumour graft surpass 2 cm in any two dimensions (according to the limits defined by the IACUC protocol), and no mouse had severe abdominal distension (≥10% increase of original body weight).

Reporting summary

Further information on research design is available in the Nature Research Reporting Summary linked to this paper.

Data availability

All data supporting the findings of this study are included in the Article and its Supplementary Information. Single-cell RNA sequencing of tumour-infiltrating immune cells were also deposited at the National Genomics Data Center (NGDC) under accession number PRJCA002149 (https://bigd.big.ac.cn/bioproject/browse/PRJCA002149). Source Data for Figs. 1–5, Extended Data Figs. 2–7, 10 are available with the paper.

28. Tu, J., Xu, M., Parvez, S., Peterson, R. T. & Franzini, R. M. Bioorthogonal removal of 3-isocyanopropyl groups enables the controlled release of fluorophores and drugs in vivo. *J. Am. Chem. Soc.* **140**, 8410–8414 (2018).
29. Rossin, R. et al. Chemically triggered drug release from an antibody–drug conjugate leads to potent antitumour activity in mice. *Nat. Commun.* **9**, 1484 (2018).
30. Zheng, Y. et al. Enrichment-triggered prodrug activation demonstrated through mitochondria-targeted delivery of doxorubicin and carbon monoxide. *Nat. Chem.* **10**, 787–794 (2018).
31. Lyon, R. P. et al. Reducing hydrophobicity of homogeneous antibody–drug conjugates improves pharmacokinetics and therapeutic index. *Nat. Biotechnol.* **33**, 733–735 (2015).
32. Liu, Z. et al. One-step ^{18}F labeling of biomolecules using organotrifluoroborates. *Nat. Protocols* **10**, 1423–1432 (2015).
33. Cheng, Y. et al. Highly efficient drug delivery with gold nanoparticle vectors for in vivo photodynamic therapy of cancer. *J. Am. Chem. Soc.* **130**, 10643–10647 (2008).
34. Duncan, B., Kim, C. & Rotello, V. M. Gold nanoparticle platforms as drug and biomacromolecule delivery systems. *J. Control. Release* **148**, 122–127 (2010).
35. De, M. et al. Sensing of proteins in human serum using conjugates of nanoparticles and green fluorescent protein. *Nat. Chem.* **1**, 461–465 (2009).
36. Rana, S., Yeh, Y. C. & Rotello, V. M. Engineering the nanoparticle–protein interface: applications and possibilities. *Curr. Opin. Chem. Biol.* **14**, 828–834 (2010).

Acknowledgements We thank J. Sui, Z. Shen, F. Zheng and P. Xu for reagents; J. Chen, F. Wang, X. Jia, Z. Jiang and W. He for technical assistance; M. Shi for the cartoon illustration; and X. Liu, P.R. Chen, T. Luo and W. Wei for advice. The work was supported by NSFC grants U1867209 and 21778003 to Z.L., NSFC Basic Science Center Project (81788104), the National Key Research and Development Program of China (2017YFA0505900 and 2016YFA0501500), Chinese Academy of Medical Sciences Initiative for Innovative Medicine (2019-I2M-5-084) to F.S.

Author contributions Z.L. and F.S. conceived the study; Q.W., assisted by C.W. and X.Z., performed material synthesis, characterization and chemical analysis; Y.W. and Q.W. performed most of the experiments; C.W. performed radiosynthesis and PET imaging; J.D., W.G. and H.H. provided technical assistance and suggestions. Q.W., Y.W., F.S. and Z.L. analysed the data. F.S. and Z.L. wrote the manuscript with input from all authors. All authors discussed the results and commented on the manuscript.

Competing interests The authors declare no competing interests.

Additional information

Supplementary information is available for this paper at https://doi.org/10.1038/s41586-020-2079-1.

Correspondence and requests for materials should be addressed to F.S. or Z.L.

Peer review information *Nature* thanks Dmitri Krysko, Andreas Linkermann and the other, anonymous, reviewer(s) for their contribution to the peer review of this work.

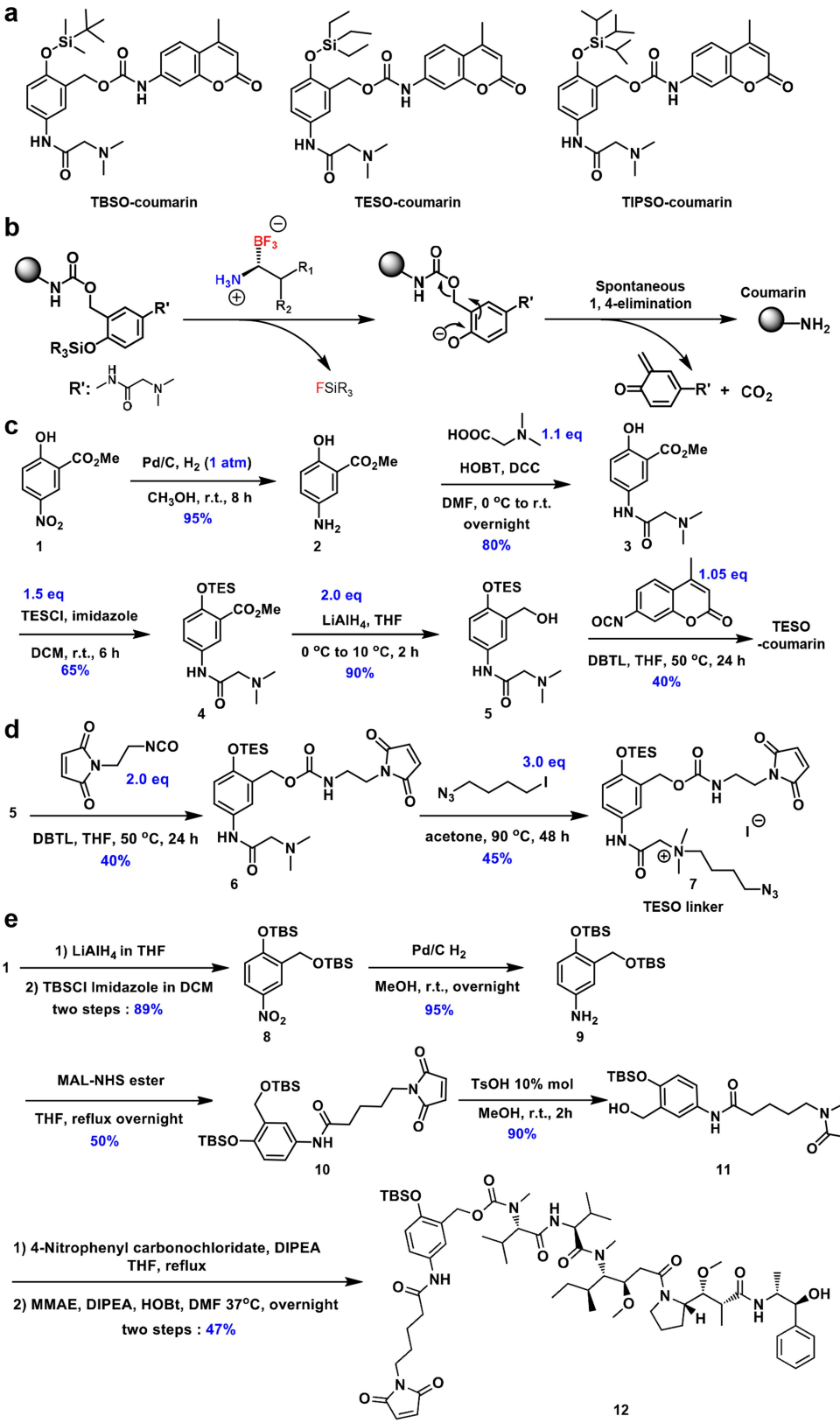

Extended Data Fig. 1 | Phe-BF_3 catalyses desilylation of carbamate linkers containing silyl ether, and synthetic routes of related compounds. **a**, Chemical structures of silyl-phenolic-ether-conjugated coumarin derivatives. **b**, Proposed mechanism for Phe-BF_3-catalysed desilylation of the silyl ether that triggers decarboxylation on the carbamate and consequent release of the coumarin. **c**, Synthetic route of TESO–coumarin. TBSO–coumarin and TIPSO–coumarin were synthesized via a similar strategy. **d**, Synthetic route of the silyl-ether-containing carbamate linker used for nanoparticle conjugation. **e**, Synthetic route of Phe-BF_3-responsive SEC–MMAE for antibody conjugation.

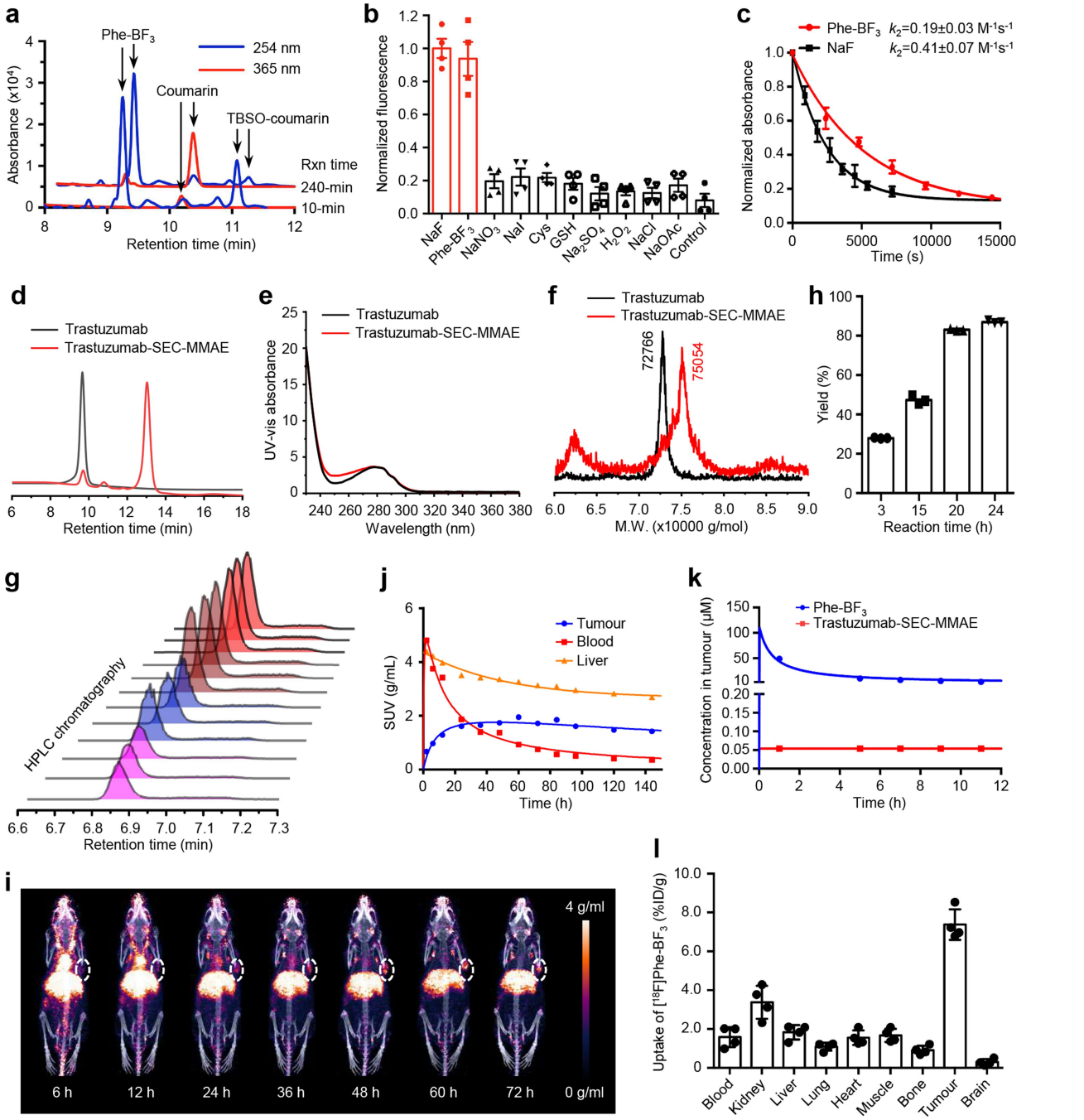

Extended Data Fig. 2 | Establishment of bioorthogonal chemistry based on desilylation that can achieve efficient and controlled MMAE release from the trastuzumab–SEC–MMAE antibody–drug conjugate system. a, Liquid chromatography (LC) assay of cleavage of TBSO–coumarin induced by Phe-BF3 desilylation. Red and blue mark the maximum absorbance wavelength of free coumarin (365 nm) and the mixtures of Phe-BF_3 and TBSO–coumarin (254 nm), respectively. **b**, Assay of possible desilylation of TBSO–coumarin (10 μM) by various biologically relevant nucleophilic anions (5 mM for GSH, 20 mM for H_2O_2 and 10 mM for others). The fluorescence intensity of coumarin (mean ± s.e.m., $n = 4$ independent replicates) was determined at $\lambda_{ex} = 370$ nm and $\lambda_{em} = 435$ nm. **c**, Determination of the rate constant of desilylation mediated by Phe-BF_3, by chromatography assay. Data shown are mean ± s.e.m. $n = 3$ independent replicates. **d**, Purity of the trastuzumab–SEC–MMAE conjugate determined by size-exclusion HPLC. **e**, **f**, UV–visible (**e**) and MALDI–TOF (**f**) analyses reveal that the drug-to-antibody ratio of trastuzumab–SEC–MMAE is approximately 4. **g**, **h**, HPLC–QTOF mass spectrometry analysis of MMAE released from trastuzumab–SEC–MMAE after incubation with Phe-BF_3 for 3 h (magenta), 15 h (blue), 20 h (brown) or 24 h (orange) in 50% serum. **h**, Quantification of the released MMAE using calibration curves. Data shown are mean ± s.e.m. $n = 3$ independent replicates. **i**–**l**, Nu/Nu mice were implanted subcutaneously with human BGC823 cancer cells. **i**, Dynamic PET computed tomography 3D projection images of mice bearing BGC823 tumours at the indicated time points after intravenous injection of [^{89}Zr]trastuzumab–SEC–MMAE. **j**, Time–activity curve (TAC) of [^{89}Zr]trastuzumab–SEC–MMAE in the blood, liver and tumour. **k**, Local concentration of Phe-BF_3 and trastuzumab–SEC–MMAE in BGC823 tumours after tail-vein injection of the corresponding agents. **l**, Ex vivo biodistribution of [^{18}F]Phe-BF_3 in mice bearing BGC823 tumours at 75 min after injection. Mean ± s.d., $n = 4$ mice. Data shown are representative of three (**a**–**i**) or two (**l**) independent experiments.

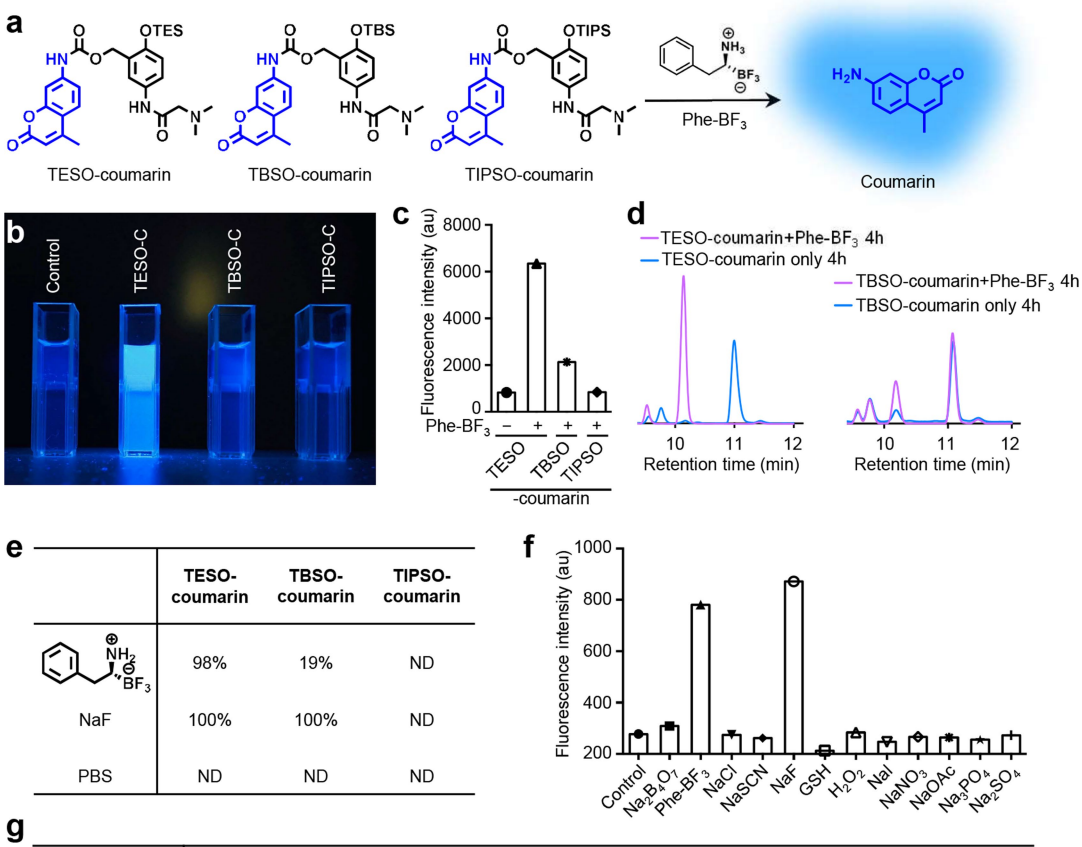

	TESO-coumarin	TBSO-coumarin	TIPSO-coumarin
Phe-BF_3	98%	19%	ND
NaF	100%	100%	ND
PBS	ND	ND	ND

Organofluorines	Phe-BF_3	FDG	Leflunomide	5-FU	Capecitabine
Name	Phe-BF_3	FDG	Leflunomide	5-FU	Capecitabine
Yield	95%	ND	ND	ND	ND

Extended Data Fig. 3 | Optimization of the silyl-ether-containing carbamate linker for higher sensitivity to Phe-BF_3. a, Schematic of Phe-BF_3-catalysed desilylation that can release the 'caged' coumarin from a designed silyl-ether-containing carbamate linker. **b**–**d**, 'Decaging' and liquid chromatography assays of Phe-BF_3-catalysed desilylation of TESO–coumarin (TESO–C), TBSO–coumarin (TBSO–C) or TIPSO–coumarin (TIPSO–C). **b**, **c**, Photographs (**b**) and quantification (**c**) of coumarin fluorescence. **d**, Blue and magenta mark the maximum absorbance wavelength of TESO–coumarin or TBSO–coumarin (254 nm) and free coumarin (365 nm), respectively. **e**, Summary of the desilylation efficiency of Phe-BF_3 and NaF towards TESO–coumarin, TBSO–coumarin or TIPSO–coumarin. **f**, Fluorescence-emission assay of possible desilylation of TESO–coumarin (10 μM) by various biologically relevant nucleophilic anions (5 mM for GSH, 20 mM for H_2O_2 and 10 mM for others). The coumarin fluorescence intensity was determined at λ_{ex} = 370 nm and λ_{em} = 435 nm. **g**, Summary of desilylation efficiency of TESO–coumarin (10 μM) by FDA-approved organofluorines. **e**, **g**, Reaction efficiency was determined by HPLC. ND, not detected. Data shown are representative of two (**c**, **f**) or three (**b**, **d**, **e**, **g**) independent experiments.

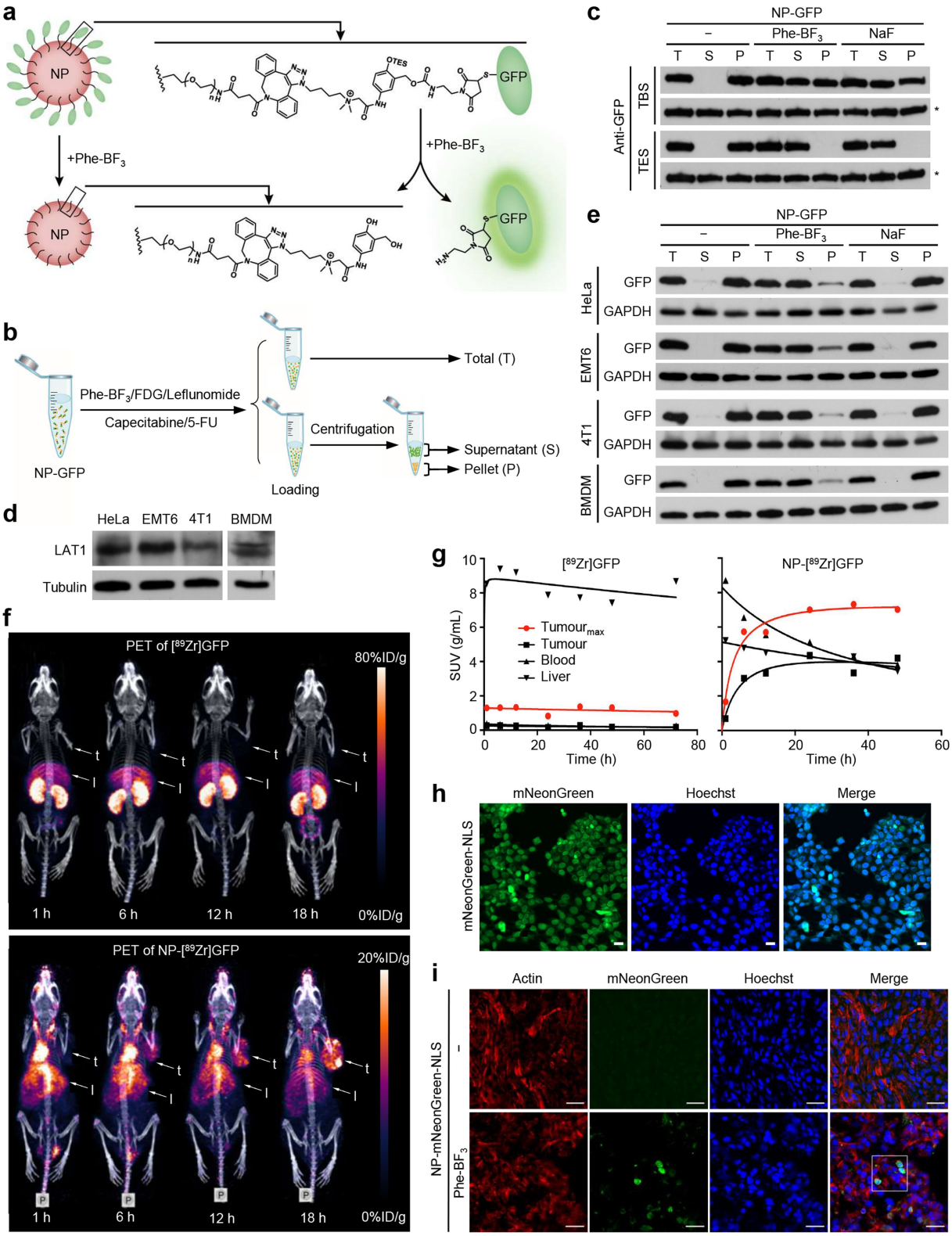

Extended Data Fig. 4 | See next page for caption.

Extended Data Fig. 4 | Release of GFP from NP–GFP induced by Phe-BF_3 desilylation, and biodistribution of [^{89}Zr]GFP and NP–[^{89}Zr]GFP in mice. **a**, Design of Phe-BF_3 desilylation of the silyl-ether-carbamate-linked NP–GFP for releasing GFP from the nanoparticle. GFP fluorescence is quenched in NP–GFP; desilylation-induced cleavage of the linker releases the GFP. **b**, Workflow of assaying release of GFP from NP–GFP induced by Phe-BF_3 desilylation in vitro. The samples were subjected to immunoblotting in **c** and Fig. 2a. **c**, Comparison of desilylation-induced release of GFP from TESO- or TBSO-linked NP–GFP by Phe-BF_3 and NaF. The loading control (*) was sampled before centrifugation. **d**, Expression of LAT1 transporter in the four cell types assayed in Extended Data Fig. 4e. **e**, Assays of release of GFP from NP–GFP induced by Phe-BF_3 desilylation in cells. HeLa, EMT6 or 4T1 cells, or primary BMDMs, were treated with NP–GFP (1 mg ml^{-1}) for 24 h and then with Phe-BF_3 (100 μM) or NaF for another 24 h. Centrifuged lysates were subjected to anti-GFP and anti-GAPDH immunoblotting. **f**, **g**, BALB/c mice were implanted subcutaneously with 4T1 cancer cells. **f**, Representative PET computed tomography 3D projection images of mice bearing 4T1 tumours at 1, 6, 12 and 18 h after intravenous injection of [^{89}Zr]GFP or NP–[^{89}Zr]GFP. **g**, Time–activity curve of [^{89}Zr]GFP and NP–[^{89}Zr]GFP in the blood, liver and tumour of mice. **h**, Representative confocal images of HeLa cells transfected with a plasmid expressing mNeonGreen–NLS. Scale bars, 20 μm. **i**, Assay of release of mNeonGreen–NLS from the NP–mNeonGreen–NLS conjugates induced by Phe-BF_3 desilylation in mice bearing 4T1 tumours. Representative confocal images of tumour sections are shown. Scale bars, 20 μm. Image in the box is magnified in Fig. 2d. Data shown in **c**–**i** are representative of two independent experiments.

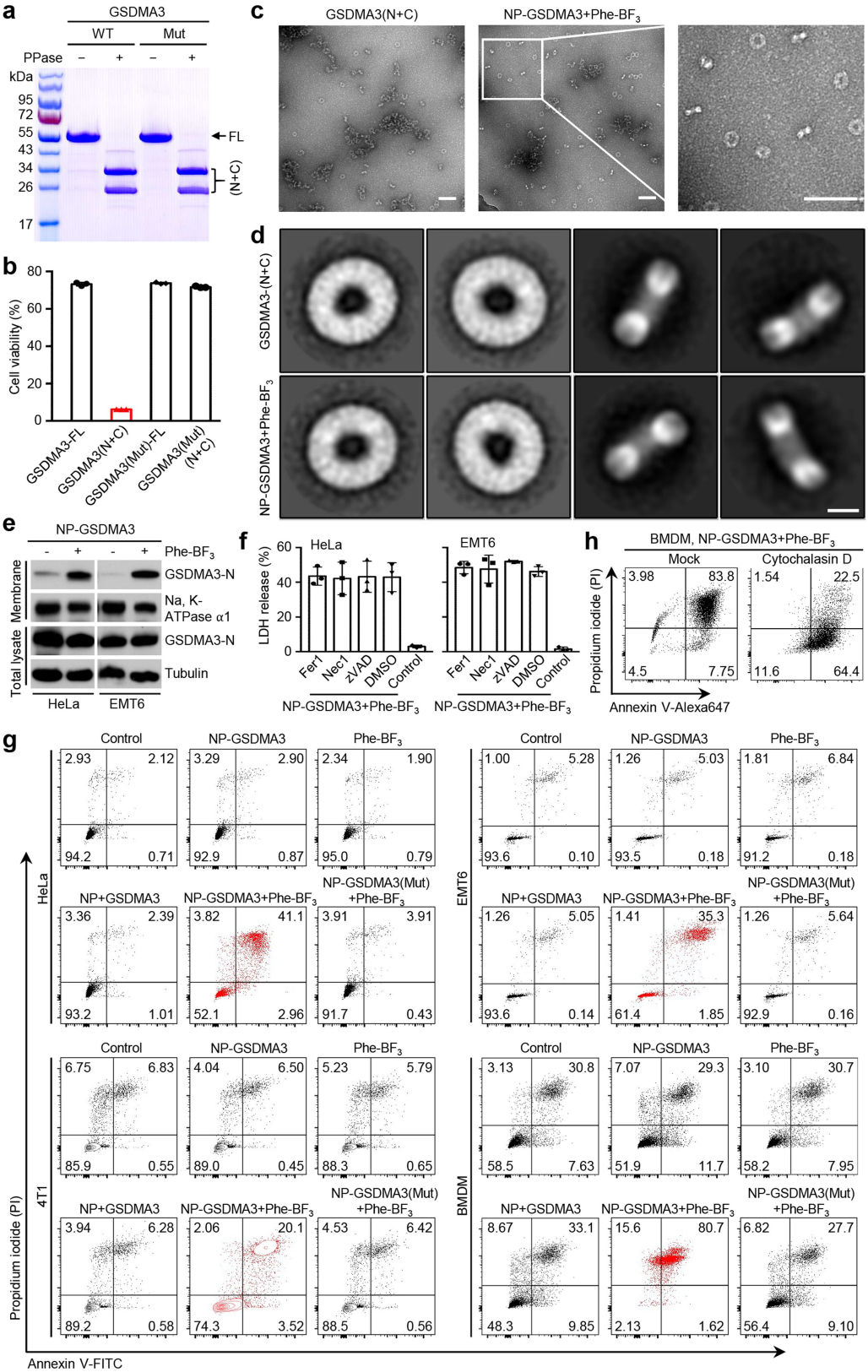

Extended Data Fig. 5 | See next page for caption.

Extended Data Fig. 5 | Phe-BF_3 desilylation of NP–GSDMA3 releases the gasdermin N domain that is capable of forming pores and inducing pyroptosis. a, **b**, Preparation of the GSDMA3(N + C) used for conjugation onto the nanoparticle. Purified GSDMA3 containing a engineered PPase cleavage site between the gasdermin N and C domain was cleaved in vitro to obtain GSDMA3(N + C). **a**, Coomassie blue staining of the prepared GSDMA3 proteins. **b**, ATP-based viability of CT26 cells electroporated with the prepared GSDMA3 protein. Mean ± s.d., $n = 3$ independent replicates. **c**, **d**, Pore-forming activity of the gasdermin N domain released from NP–GSDMA3 by desilylation catalysed by Phe-BF_3. **c**, Representative negative-stain electron microscopy images of the gasdermin pores formed by purified native GSDMA3(N + C) protein or the GSDMA3(N + C) protein released from NP–GSDMA3. Scale bars, 100 nm. **d**, Representative 2D averages of the gasdermin pores viewed from the top (left) and the side (right). Scale bar, 10 nm. **e**, **f**, HeLa or EMT6 cells were treated with NP–GSDMA3 alone or in combination with Phe-BF_3. **e**, Total cell lysates or their membrane fractions were immunoblotted with indicated antibodies. Flag–GSDMA3(N + C) proteins (the Flag tag was fused C-terminal to the gasdermin N domain, before the PPase cleavage site) were conjugated to the nanoparticle. The GSDMA3 N domain was probed by anti-Flag immunoblotting. **f**, LDH assay of the effect of various inhibitors on cell death induced by treatment with NP–GSDMA3 and Phe-BF_3. Mean ± s.d., $n = 3$ independent replicates. Fer1, ferrostatin 1; Nec-1, necrostatin 1. **g**, HeLa, EMT6 or 4T1 cells, or primary BMDMs, were treated as indicated. NP + GSDMA3, nanoparticles mixed with the noncovalent GSDMA3(N + C) complex. GSDMA3(Mut), the pore forming-deficient E14K/L184D mutant version of GSDMA3(N + C). Flow-cytometry plots of PI- and annexin V–-FITC-stained cells are shown. **h**, Effect of phagocytosis inhibitor cytochalasin D on cell death induced by treatment with NP–GSDMA3 and Phe-BF_3 in primary BMDMs. Flow-cytometry plots of PI- and annexin V–Alexa-647-stained cells are shown. Data are representative of two (**c**–**f**, **h**) or three (**a**, **b**, **g**) independent experiments.

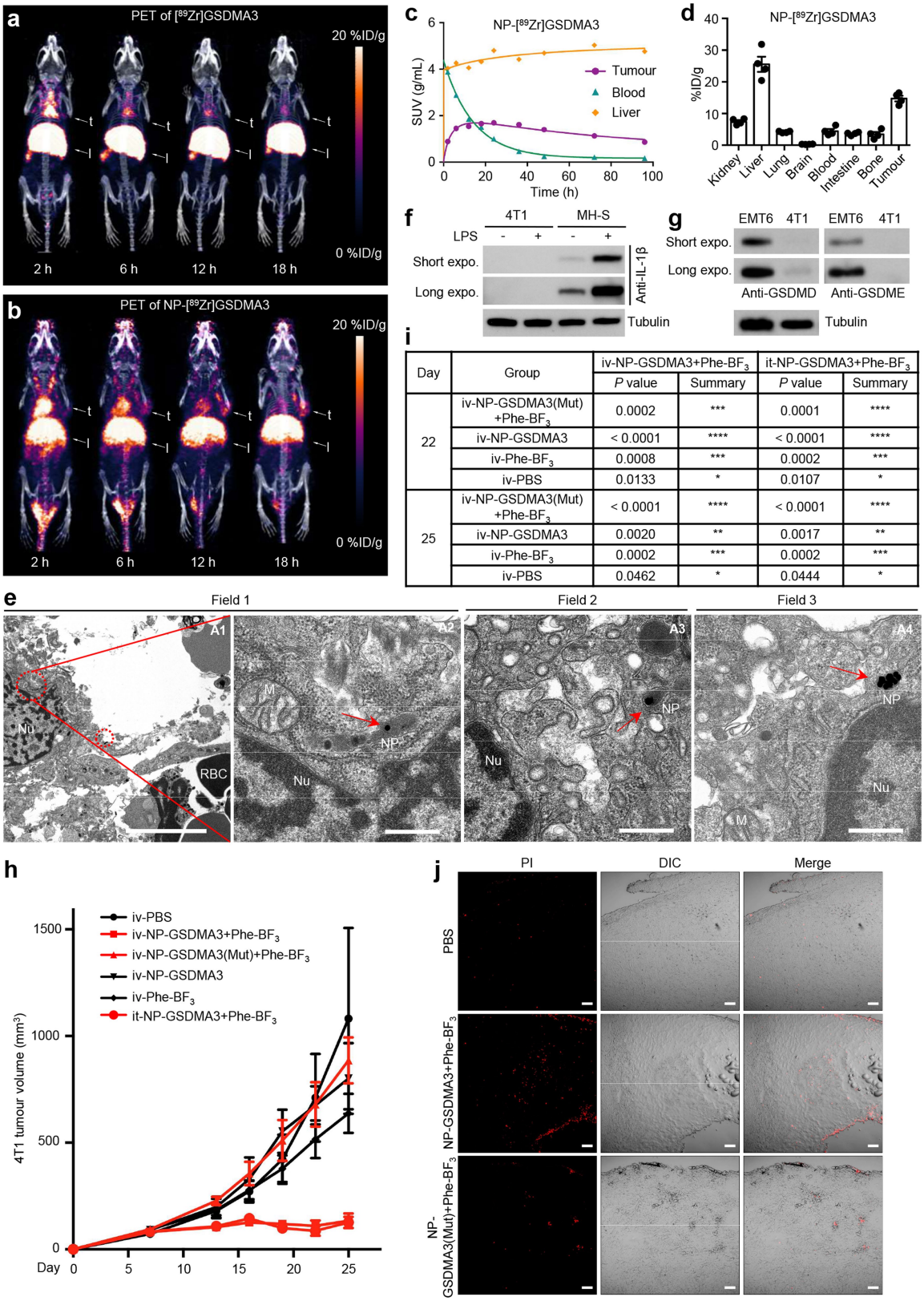

Day	Group	iv-NP-GSDMA3+Phe-BF_3		it-NP-GSDMA3+Phe-BF_3	
		P value	Summary	*P* value	Summary
22	iv-NP-GSDMA3(Mut) +Phe-BF_3	0.0002	***	0.0001	****
	iv-NP-GSDMA3	< 0.0001	****	< 0.0001	****
	iv-Phe-BF_3	0.0008	***	0.0002	***
	iv-PBS	0.0133	*	0.0107	*
25	iv-NP-GSDMA3(Mut) +Phe-BF_3	< 0.0001	****	< 0.0001	****
	iv-NP-GSDMA3	0.0020	**	0.0017	**
	iv-Phe-BF_3	0.0002	***	0.0002	***
	iv-PBS	0.0462	*	0.0444	*

Extended Data Fig. 6 | See next page for caption.

Extended Data Fig. 6 | Biodistribution and cytodistribution of NP–[^{89}Zr]GSDMA3, and effect of treatment with NP–GSDMA3 and Phe-BF_3 on mice bearing 4T1 tumours. a–**e**, BALB/c mice were implanted subcutaneously with 4T1 cancer cells, and intravenously injected with [^{89}Zr]GSDMA3 or NP–[^{89}Zr]GSDMA3. **a**, **b**, PET computed tomography 3D projection images of mice bearing 4T1 tumours at the indicated time points after injection of [^{89}Zr]GSDMA3 or NP–[^{89}Zr]GSDMA3. **c**, Time–activity curve of NP–[^{89}Zr]GSDMA3 in the blood, liver and tumour of injected mice. **d**, Systemic biodistribution of NP–[^{89}Zr]GSDMA3 in mouse tissues. Data shown are mean ± s.e.m. $n = 4$ mice. **e**, Representative transmission electron microscopy images showing the cytodistribution of NP–GSDMA3 in the 4T1 tumour tissue. Nu, nucleus; M, mitochondrion; NP, nanoparticle; RBC, red blood cell. Scale bars, 5 µm (A1), 500 nm (A2–A4). **f**, **g**, Immunoblotting assay of endogenous IL-1β, GSDMD and GSDME expression. **f**, 4T1 or MH-S cells were stimulated with LPS (2 µg ml^{-1}) for 12 h and the cell lysates were subjected to anti-IL-1β or anti-tubulin immunoblotting. **g**, Lysates of EMT6 and 4T1 cells were blotted with anti-GSDMD, anti-GSDME or anti-tubulin antibodies. **h**, **i**, Mice bearing 4T1 tumours were treated with NP–GSDMA3 and Phe-BF3, as depicted in Fig. 4b ($n = 7$ mice for each group). Average tumour volumes of each group of mice at the indicated time points after the injection are shown as mean ± s.e.m. (in **h**) with *P* values in **i** (two-tailed unpaired Student's *t*-test). **j**, Propidium iodide staining of tumour-cell pyroptosis induced by treatment with NP–GSDMA3 and Phe-BF_3 in mice. An independent experiment from that shown in Fig. 5a. Scale bars, 100 µm. All data shown are representative of two (**a**–**g**, **j**) or three (**h**, **i**) independent experiments.

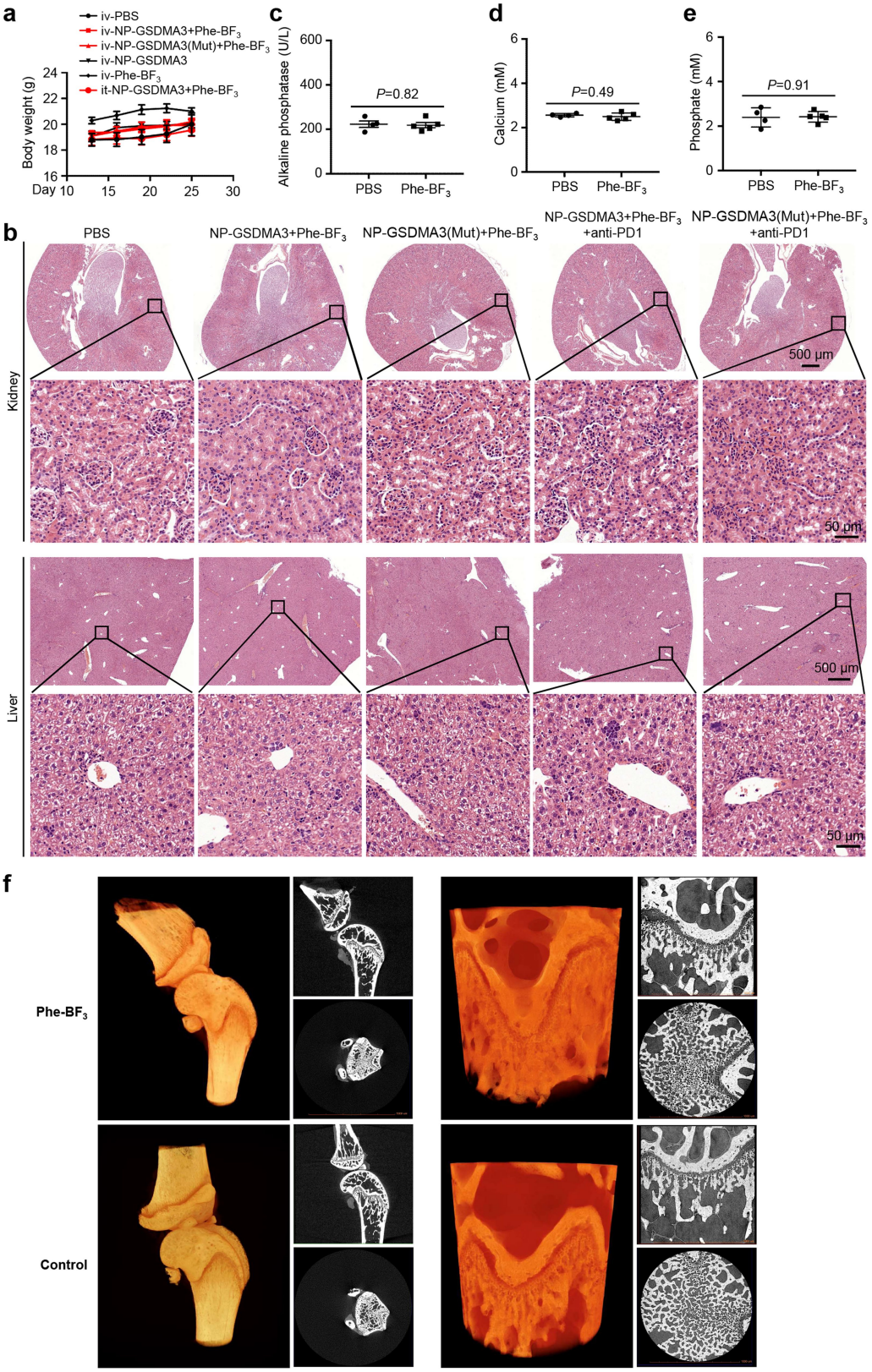

Extended Data Fig. 7 | See next page for caption.

Extended Data Fig. 7 | Evaluation of the possible side effects of treatment with NP–GSDMA3 and Phe-BF_3 in mice. a, Records of mouse body weight after the indicated treatments. Data shown are mean ± s.e.m. $n = 8$ mice for PBS, NP–GSDMA3, Phe-BF_3 and intratumourally injected NP–GSDMA3 + Phe-BF3, 9 mice for NP–GSDMA3 + Phe-BF3 and NP–GSDMA3(mut) + Phe-BF_3. **b**, Representative haematoxylin and eosin (H & E) staining of liver and kidney tissues from mice with indicated treatments. Three mice per group. **c**–**e**, Assay of serum concentrations of alkaline phosphatase, calcium and phosphate in mice treated with PBS ($n = 4$ mice) or Phe-BF_3 ($n = 5$ mice). Data shown are mean ± s.e.m. Two-tailed unpaired Student's *t* test. **f**, Normal-resolution (left) and high-resolution (right) computed tomography scans of the joint from mice treated with Phe-BF_3 or PBS. For the normal-resolution scan, a 3D reconstruction image of the whole joint is shown on the left; representative 2D images of the sagittal plane (top) and axial plane near the femur growth plate (bottom) are shown on the right. For the high-resolution computed tomography scan that images a voxel near the femur growth plate, the whole voxel is shown on the left and representative images of the sagittal plane (top) and the axial plane (bottom) are shown on the right. Data are representative of three (**a**) or two (**b**–**f**) independent experiments.

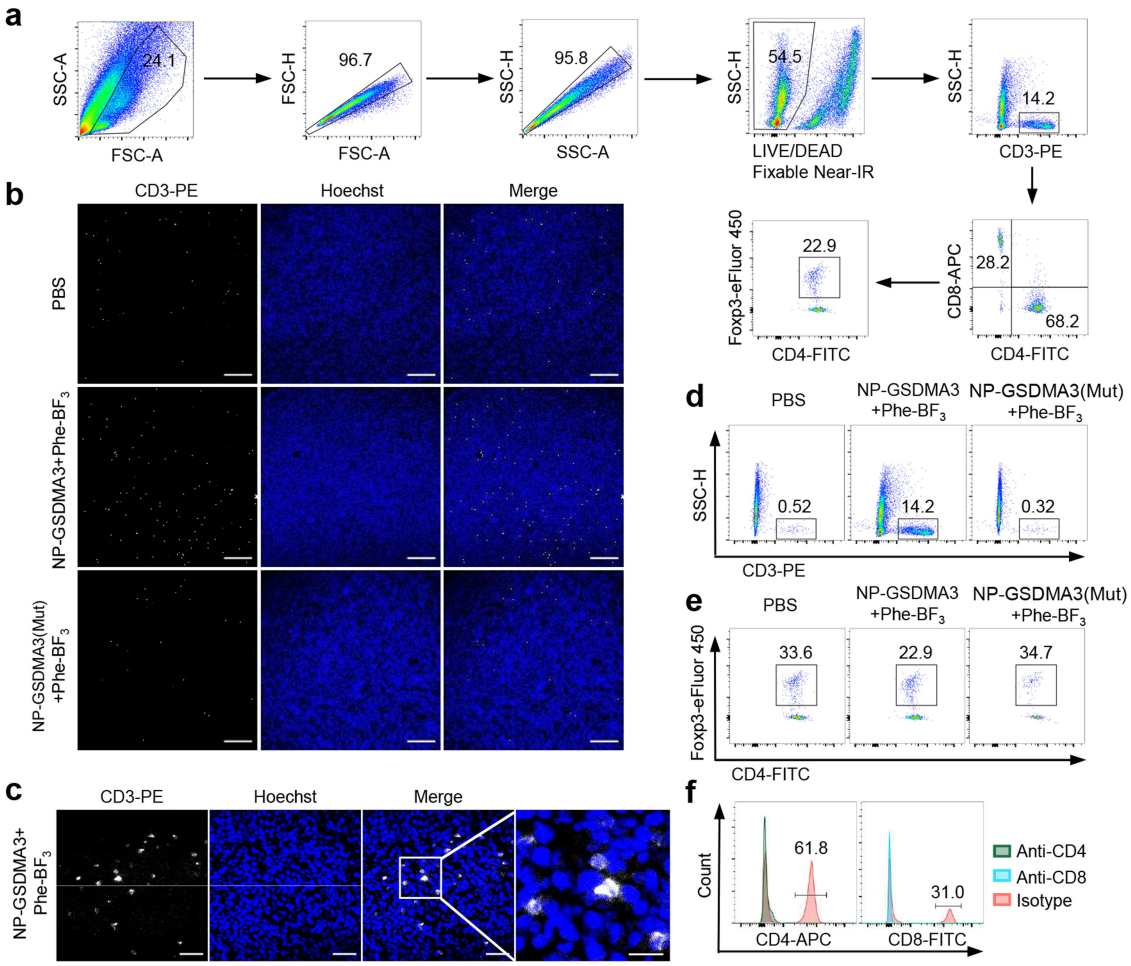

Extended Data Fig. 8 | Pyroptosis induced by NP–GSDMA3 and Phe-BF_3 stimulates inflammation and increases the tumour-infiltrating lymphocytes. a, **d**, **e**, Gating strategy (**a**) and representative flow-cytometry plots for assessing 4T1 tumour-infiltrating $CD3^+$ T cells (**d**) or $FOXP3^+CD4^+$ regulatory T cells (**e**) following the indicated treatments. **b**, **c**, Representative fluorescence images of CD3–PE-stained 4T1 tumours following treatment with PBS ($n = 4$ mice), NP–GSDMA3 and Phe-BF_3 ($n = 4$ mice) or NP–GSDMA3(mut) and Phe-BF_3 ($n = 6$ mice). Scale bars, 200 μm (**b**), 50 μm (**c**, left), 20 μm (**c**, right). **f**, Flow-cytometry analysis of $CD4^+$ or $CD8^+$ T cells upon depletion by their corresponding antibody. Data shown are representative of two (**b**, **c**, **f**) or three (**a**, **d**, **e**) independent experiments.

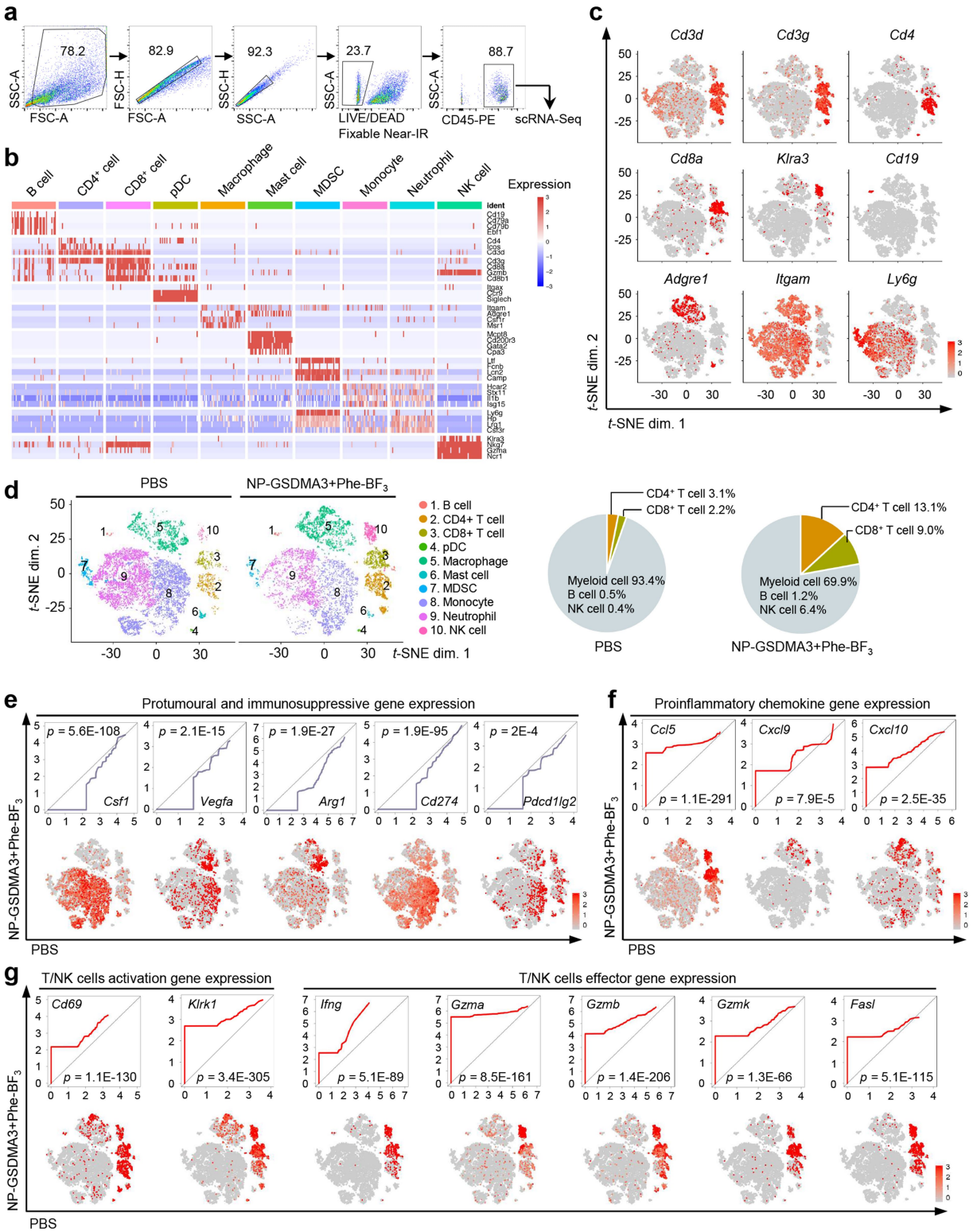

Extended Data Fig. 9 | Tumour-infiltrating immune-cell-subtype analysis by single-cell RNA sequencing. a, Gating strategy and representative flow-cytometry plots for the enrichment of 4T1 tumour-infiltrating single CD45$^+$ immune cells. **b**, Heat map of ten immune-cell clusters with unique signature genes. Colours on top of the map indicate the immune-cell clusters. The three or four marker genes used for each cluster are listed alongside the cluster. **c**, Signature gene-expression patterns for the corresponding cell clusters on the *t*-SNE plot ($n = 4,18,069$ cells). **d**, *t*-SNE plots of tumour-infiltrating single CD45$^+$ immune cells of 4T1 tumours from mice treated with PBS ($n = 2$ mice, 10,171 cells) or NP–GSDMA3 and Phe-BF$_3$ ($n = 2$ mice, 7,898 cells) (left), and the relative frequencies of different clusters (right). **e**–**g**, Expression levels of protumoural and immunosuppressive genes (**e**), proinflammatory chemokine (**f**) and T and/or natural killer cell activation or effector (**g**) genes in immune cells. Paired quantile–quantile (*Q*–*Q*) plots were used to compare the gene-expression levels in CD45$^+$ immune cells between 4T1 tumours treated with PBS or NP–GSDMA3 and Phe-BF$_3$. *P* values were calculated using a two-sided Wilcoxon rank-sum test. All data are representative of two independent experiments.

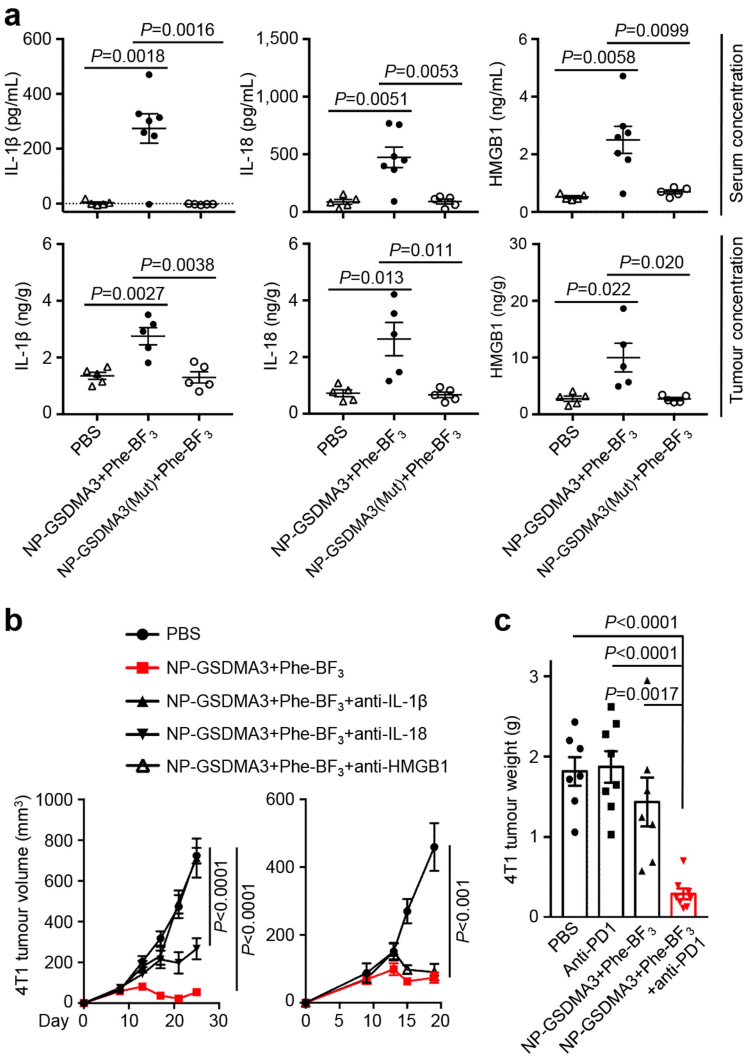

Extended Data Fig. 10 | Antitumour immunity activated by NP–GSDMA3 and Phe-BF_3 requires IL-1β, and can synergize with the anti-PD1 therapy. a, Enzyme-linked immunosorbent assay measurements of IL-1β, IL-18 and HMGB1 concentration in the serum (top) and the tumour homogenates (bottom) of mice treated with PBS, NP–GSDMA3 and Phe-BF_3 or NP–GSDMA3(mut) and Phe-BF_3 ($n = 5$ or 7, as shown in the figure for each group). **b**, Anti-IL-1β, IL-18 or HMGB1 antibodies were intraperitoneally injected into mice bearing 4T1 tumours, before treatment with NP–GSDMA3 and Phe-BF_3 ($n = 7$ mice each group). Mice bearing 4T1 tumours were also treated with PBS alone as the control group ($n = 8$). Average tumour volumes at the indicated time points after implantation are shown. **c**, Mice bearing 4T1 tumours were treated with PBS ($n = 7$ mice), anti-PD1 ($n = 8$ mice) or NP–GSDMA3 and Phe-BF3 ($n = 7$ mice) alone, or in combination ($n = 8$ mice) as shown in Fig. 5i. All data are shown as mean ± s.e.m. (two-tailed unpaired Student's *t*-test) and are representative of two independent experiments.

nature research

Corresponding author(s): Feng Shao

Life Sciences Reporting Summary

Nature Research wishes to improve the reproducibility of the work that we publish. This form is intended for publication with all accepted life science papers and provides structure for consistency and transparency in reporting. Every life science submission will use this form; some list items might not apply to an individual manuscript, but all fields must be completed for clarity.

For further information on the points included in this form, see Reporting Life Sciences Research. For further information on Nature Research policies, including our data availability policy, see Authors & Referees and the Editorial Policy Checklist.

Please do not complete any field with "not applicable" or n/a. Refer to the help text for what text to use if an item is not relevant to your study.
For final submission: please carefully check your responses for accuracy; you will not be able to make changes later.

Experimental design

1. Sample size

   Describe how sample size was determined.

   No statistical methods were used to predetermine the sample sizes. It is impossible to predict the magnitude of experimental variation between animals based on our current knowledge. The group sizes (at least three animals per treatment group) represents the minimum number animals needed to reach statistical significance ($p < 0.05$) between experimental groups.

2. Data exclusions

   Describe any data exclusions.

   There were no data exclusions.

3. Replication

   Describe the measures taken to verify the reproducibility of the experimental findings.

   All attempts at replication are successful. Experiments results were robust and reproducible. The difference between the treated group and control group were statistically significant in the repetitive experiments.

4. Randomization

   Describe how samples/organisms/participants were allocated into experimental groups.

   No randomization was used in this study. For all in vivo experiments, animals were randomly assigned into a treatment group after tumour inoculation. The starting tumour burden in the treatment and control groups was similar before treatment.

5. Blinding

   Describe whether the investigators were blinded to group allocation during data collection and/or analysis.

   No blinding was done in this study. Most of the studies contained multiple steps (including the material preparation, mouse tumour treatment, and so on) and the scientists must keep careful track of conditions. It would be exceedingly difficult to blind such studies.

Note: all in vivo studies must report how sample size was determined and whether blinding and randomization were used.

6. Statistical parameters

For all figures and tables that use statistical methods, confirm that the following items are present in relevant figure legends (or in the Methods section if additional space is needed).

n/a	Confirmed
☐	☒ The exact sample size (*n*) for each experimental group/condition, given as a discrete number and unit of measurement (animals, litters, cultures, etc.)
☐	☒ A description of how samples were collected, noting whether measurements were taken from distinct samples or whether the same sample was measured repeatedly
☐	☒ A statement indicating how many times each experiment was replicated
☐	☒ The statistical test(s) used and whether they are one- or two-sided *Only common tests should be described solely by name; describe more complex techniques in the Methods section.*
☐	☒ A description of any assumptions or corrections, such as an adjustment for multiple comparisons
☐	☒ Test values indicating whether an effect is present *Provide confidence intervals or give results of significance tests (e.g. P values) as exact values whenever appropriate and with effect sizes noted.*
☐	☒ A clear description of statistics including central tendency (e.g. median, mean) and variation (e.g. standard deviation, interquartile range)
☐	☒ Clearly defined error bars in all relevant figure captions (with explicit mention of central tendency and variation)

See the web collection on statistics for biologists for further resources and guidance.

Software

Policy information about availability of computer code

7. Software

Describe the software used to analyze the data in this study.

Videos were processed using the Volocity software (PerkinElmer). All the flow cytometry data were processed using FlowJo (version 10.4.0, Becton, Dickinson & Company).

For manuscripts utilizing custom algorithms or software that are central to the paper but not yet described in the published literature, software must be made available to editors and reviewers upon request. We strongly encourage code deposition in a community repository (e.g. GitHub). *Nature Methods* guidance for providing algorithms and software for publication provides further information on this topic.

Materials and reagents

Policy information about availability of materials

8. Materials availability

Indicate whether there are restrictions on availability of unique materials or if these materials are only available for distribution by a third party.

All unique materials used are readily available from the authors.

9. Antibodies

Describe the antibodies used and how they were validated for use in the system under study (i.e. assay and species).

PE-conjugated anti-mouse CD3 (Cat # 100206, clone 17A2, Lot: B257196, 1:100), FITC-conjugated anti-mouse CD4 (Cat # 100510, clone RM4.5, Lot: B245229, 1:100), and APC-conjugated anti-mouse CD8 (Cat # 100712, clone 53-6.7, Lot: B244174, 1:100) were purchased from BioLegend. eFluor 450-conjugated anti-mouse Foxp3 antibody (Cat # 14-5773-82, clone FJK-16s, Lot: 4332193, 1:100) was obtained from Invitrogen. Trastruzumab antibody used to generate the ADC was a gift from Beijing People's Hospital. The PD1 antibody used for treating 4T1 tumours was a gift from BeiGene. For immune cell depletion, anti-mouse CD4 (Cat # BE0003-1, clone GK1.5, Lot: 699918O1B) and isotype control (Cat # BE0090, clone LTF-2, Lot: 695618J2) antibodies were produced by BioXcell, and anti-mouse CD8 was a gift from Dr. J. Sui (National Institute of Biological Sciences, Beijing). Anti-LAT1 antibody (Cat # sc-374232, D-10, Lot: C0518, 1:1000) was obtained from Santa Cruz Biotechnology. Anti-GFP was a gift from Dr. Ting Han (National Institute of Biological Sciences, Beijing), originally purchased from Roche (Cat # 11814460001, 1:5000). Anti-Na, K-ATPase α1 was a gift from Dr. Xiaodong Wang (National Institute of Biological Sciences, Beijing), originally purchased from Epitomics (Cat # 2047-1, 1:1000). Anti-GAPDH (Cat # G8795, 1:5000) and anti-Flag (Cat # F1804, D-10, Lot: 124K6106, 1:5000) antibodies were purchased from Sigma-Aldrich. Anti-GSDME (Cat # ab215191, 1:1000) and anti-GSDMD (Cat # ab219800, 1:1000) were from Abcam. Anti-IL-1β (Cat # GTX74034, Lot: 42900, 1:1000) was obtained from Genetex.

All antibodies for FACS and immune cell depletion were well-recognized clones in the field and validated by the manufacturers. These antibodies are further validated and routinely used in our lab. Antibodies targeting GFP, LAT1, Na, K-ATPase α1, GAPDH, GSDMD, GSDME, IL-1β, and Flag were validated by immunoblotting and all the detected-bands were matched with the predicted molecular weight.

10. Eukaryotic cell lines

a. State the source of each eukaryotic cell line used.

HeLa and mouse EMT6 and CT26 cells were obtained from the American Type Culture Collection (ATCC). Mouse mammary carcinoma 4T1 cells were obtained from the China Infrastructure of Cell Line Resources (Chinese Academy of Medical Sciences, Beijing, China). Primary bone marrow-derived macrophage (priBMDM) cells were prepared and cultured by following a standard protocol as previously described (Reference 4)

b. Describe the method of cell line authentication used.

Identity of the cell lines were frequently checked by their morphological features but have not been authenticated by the short tandem repeat (STR) profiling.

c. Report whether the cell lines were tested for mycoplasma contamination.

All cell lines were tested to be mycoplasma-negative by the standard PCR method.

d. If any of the cell lines used are listed in the database of commonly misidentified cell lines maintained by ICLAC, provide a scientific rationale for their use.

No commonly misidentified cell lines are used in this study.

Animals and human research participants

Policy information about studies involving animals; when reporting animal research, follow the ARRIVE guidelines

11. Description of research animals

Provide all relevant details on animals and/or animal-derived materials used in the study.

6-8 week-old female mice (BALB/c background or the Nu/Nu nude mice) were used for all animal experiments described in this study.

Policy information about studies involving human research participants

12. Description of human research participants

Describe the covariate-relevant population characteristics of the human research participants.

There are no human subjects involved in this study.